Pre-print, January 4, 2005

Observed Variability of Ocean Wave Stokes Drift, and the Eulerian Response to Passing Groups

Jerome A. Smith

Scripps Institution of Oceanography, La Jolla, CA 92093

Date Received: .

Corresponding author address:

Dr. J. A. Smith
Scripps Institution of Oceanography
UCSD, mail stop 0213
9500 Gilman Dr.
La Jolla, CA, 92093-0213
Email: jasmith@ucsd.edu

Short Title:

Stokes Drift and Eulerian Response

Jerome A. Smith

ABSTRACT

Waves and currents interact via exchanges of mass and momentum. The mass and momentum fluxes associated with surface waves are closely linked to their Stokes drift. Both the variability of the Stokes drift and the corresponding response of the underlying flow are important in a wide range of contexts. Three methods are developed and implemented to evaluate Stokes drift from a recently gathered oceanic data set, involving surface velocities measured continually over an area 1.5 km in radius by 45°. The estimated Stokes drift varies significantly, in line with the occurrence of compact wave groups, resulting in highly intermittent maxima. One method involves estimation of currents at a fixed level (i.e., Eulerian); it is found that Eulerian counter-flows occur that completely cancel the Stokes drift variations at the surface. Thus the estimated fully Lagrangian surface flow has no discernable mean response to wave group passage.

1. Introduction

Surface waves are of central importance to air-sea interactions in general [e.g. see *Thorpe*, 1982; *Edson and Fairall*, 1994; *Andreas et al.*, 1995; *Asher et al*., 1996; *Pattison and Belcher*, 1999; *Zilitinkevich et al.*, 2001; *Zappa et al*., 2004], and in particular to the motion in the surface layer of the sea. For example, much of the wind stress acts directly on the waves, which then transmit the stress to the underlying flow via intermittent wave-breaking events. Although it has historically been the subject of much discussion, the implications of this intermittent stress transfer have only recently been simulated and studied in detail [*Sullivan et al.*, 2004]. The simulations indicate that vortical structures resulting from breaking events influence the motion to a depth many times greater than the wave amplitude, deeper than previously thought.

It has long been recognized that waves transport mass and momentum [*Stokes*, 1847; *Longuet-Higgins*, 1953]. Both can be related to the difference between the average velocity of a fluid parcel (Lagrangian velocity) relative to the current as measured at a fixed point (Eulerian velocity). This difference, first identified by *Stokes* [1847], is called the “Stokes drift.” The vertical integral of the Stokes drift is the “Stokes transport,” corresponding to both the net mass-flux and wave momentum per square meter of surface [*Longuet-Higgins and Stewart*, 1962]. As waves are strained and refracted by currents, exchanges of mass and momentum occur between the waves and mean flow. *Longuet-Higgins and Stewart* [1962, 1964], described the “excess flux of momentum due to the presence of waves” and, in analogy to optics, named it the “radiation stress” (noting a slight grammatical inconsistency but bowing to historical usage). Changes in the radiation stress (momentum flux) of the waves are compensated for by changes in the mean field, so the overall momentum is conserved. Additional analysis is needed to determine the partitioning of momentum between waves and the mean. For example, earlier papers [*Longuet-Higgins and Stewart*, 1960, 1961] provided the basis to describe the generation of group-bound forced long waves, which is relevant to the “Eulerian response” discussed here. Such wave-current interactions are also thought important in generating and maintaining Langmuir circulation, a prominent form of motion found in the wind-driven surface mixed layer [*Langmuir*, 1938; *Craik and Leibovich*, 1976; *Craik*, 1977; *Leibovich*, 1977; *Leibovich*, 1980;

Phillips, 2002]. Analyses and simulations indicate that LC is important in the long-term evolution of the mixed layer [*Li et al.*, 1995; *Skyllingstad and Denbo*, 1995; *McWilliams et al.*, 1997; *McWilliams and Sullivan*, 2000]. A key term in the generating interaction involves the bending of vortex lines by the vertically non-uniform Stokes drift of the waves. Thus, it is desirable to estimate the depth-dependence of the Stokes drift, including possible variations in direction as well as magnitude.

To date, analyses and simulations of Langmuir circulation have considered only the overall mean Stokes drift due to the waves. However, given that the intermittent nature of wave breaking in transmitting stress to the underlying flow has recently been found important [*Sullivan et al.*, 2004], it's reasonable to examine the spatial and temporal scales over which the Stokes drift varies, since there may be an analogous effect.

Evaluation of Stokes drift from a recently gathered oceanic data set is one focus of this paper. The experiment took place just off the WNW shore of Oahu (Hawaii, USA). An area of the ocean surface roughly 1.5 km radius by 45° in bearing was monitored for velocity and acoustic backscatter intensity, using a novel acoustic Doppler system referred to as the "Long-Range Phased-Array Doppler Sonar" (LRPADS). The area is resolved to 7.5 m in range by 1.3° in bearing (~7000 cells), sampled every 2.5 s. The vertical aperture encompasses the ocean surface and the near-surface bubble layer, which almost always dominates in backscatter intensity by several orders of magnitude over returns from all other depths, and yields a vertical scale-depth for the measurement of about 1.5 m.

Another focus is examination of the underlying flow field. One method developed here for Stokes drift ("method 3") involves estimating currents at both a fixed level (Eulerian) and following the surface (semi-Lagrangian: following vertical but not horizontal displacements). It is found that Eulerian counter-flows occur that cancel the estimated Stokes drift variations at the surface completely. The estimated fully Lagrangian surface flow shows no discernable mean response to wave group passage. This is a stronger surface response than expected from the group-bound forced wave analysis mentioned above (discussed further in section 7 here). However, similar sized Eulerian counter-flows have been observed in laboratory experiments (e.g., *Klopman* 1994, as referenced in [*Groeneweg and Klopman*, 1998]; also *Kemp and Simons* [1982, 1983]; *Swan* [1990]; *Jiang and Street* [1991]; *Monismith et al.* [1996]; and others). The most rigorous treatment is that of *Groeneweg and Klopman*,

[1998], who develop a numerical model employing a "Generalized Lagrangian Mean" (GLM) formulation [*Andrews and McIntyre*, 1978; *Grimshaw*, 1981], including finite shear and turbulence. The changes in current profile from case to case (no waves, down-current waves, up-current waves) are comparable to the Stokes drift profile calculated from the wave parameters as given (in both magnitude and shape), although this comparison was not explicitly made. Wave-group responses in the field have been observed previously via pressure arrays in finite-depth water [*Herbers et al.*, 1994], and were found to be consistent with 2nd order theory for that case; however, the expected response in intermediate depths differs markedly from that in deep water, so a detailed comparison may not be appropriate. The observations presented here are the first concerning the Eulerian current response in open ocean, deep-water conditions (> 1000 m depth). The results suggest that, at least at the surface, the one-to-one balance between the Stokes drift and the induced horizontal Eulerian counter-flow at the surface may be a general result, not confined to the laboratory setting.

Organization of the paper is as follows: (1) This introduction. (2) Definition of Stokes transport and drift, with an eye toward evaluation from measured directional wave spectra. (3) Experimental setting and circumstances. (4) Area-mean estimates of surface Stokes drift from the difference between the mean velocity of features embedded in the surface flow (bubble clouds) versus the mean Doppler shift, including analysis of acoustic sheltering of wave crests. (5) Time-range and wavenumber-frequency analysis, and development of two more methods to estimate the Stokes drift using k-f Fourier coefficients. (6) Observed Eulerian and Lagrangian responses, estimated as described. (7) Discussion, including estimates of the expected (irrotational) response. (8) Results and Conclusions.

2. Stokes Drift Due to the Surface Waves

To set the stage and clarify terminology, the Stokes drift is defined and some of its characteristics are described for the case of deep water surface waves. Both the volume transport and the Stokes drift profile due to the presence of waves are considered, and the stage is set to estimate the time-space variations of Stokes drift and transport from data.

2.1. Stokes Transport and Linear Waves

In an Eulerian frame, the Stokes transport arises entirely at the moving surface. For simplicity, the density is assumed constant, and set to 1. Taylor-expanding from the mean surface at z = 0,

$$
\begin{aligned}
\mathbf{T}^S &\equiv \overline{\int_{-h}^{\zeta} \mathbf{u}(z)\, dz} - \int_{-h}^{\bar{\zeta}} \overline{\mathbf{u}(z)}\, dz = \overline{\int_{0}^{\zeta} \mathbf{u}(z)\, dz} - \int_{0}^{\bar{\zeta}} \overline{\mathbf{u}(z)}\, dz \\
&\approx \overline{\int_0^{\zeta} \{\mathbf{u}(0) + z\partial_z \mathbf{u}(0) + \ldots\}\, dz} \approx \{\, \overline{\zeta \mathbf{u}'} + \tfrac{1}{2}\overline{\zeta^2}\partial_z \bar{\mathbf{u}} + \ldots\}_{z=0} \\
&\approx \overline{\zeta \mathbf{u}'}\,|_{z=0}
\end{aligned}
\tag{2.1}
$$

The mixed-term involving mean vertical shear is assumed small. The linearized momentum equation at the surface, again expanding from z = 0, is used to complete the evaluation. Aligning the wave with the x-axis so that $\mathbf{u} = u$, and substituting a wave-solution of the form $P e^{i(kx - \sigma t)}$ for both ζ and u,

$$
\partial_t u + g\, \partial_x \zeta = (-i\sigma)u + g(ik)\zeta \quad \text{or} \quad u = \sigma\zeta \tag{2.2}
$$

where use is made of the linear dispersion relation in the absence of currents, $\sigma^2 = gk$. Thus, the net Stokes transport is

$$
\mathbf{T}^S \approx \overline{\zeta u} = \sigma \overline{\zeta^2} = \overline{u^2} / \sigma \tag{2.3}
$$

For waves propagating in weak shear, the Stokes transport can be identified to second order in wave slope with the wave momentum.

2.2. Stokes Drift Profile

Theories describing wave/current interactions generally require not just the integrated transport, but the vertical profile of Stokes drift. To determine this, the notion of “displacement” is extended to the fluid interior, and also to include the horizontal displacements associated with the waves. The displaced location of a fluid parcel is associated with its undisplaced location; i.e., for some function of space-time “q,” associate

$$q^L(x,z,t) \Leftrightarrow q(x+\chi, z+\zeta, t) \tag{2.5}$$

following *Andrews and McIntyre* [1978a] (note there is an implicit assumption that the mapping is unique and invertible; also, the Jacobean of this transformation might not be one).

The Generalized Lagrangian Mean (GLM; c.f. *Andrews and McIntyre* [1978a]) is formed over the displaced locations, while the Eulerian mean is formed (as normally done) at the undisplaced location:

$$\bar{q}^L = \overline{q(x+\chi,\, z+\zeta,\, t)} \quad \text{and} \quad \bar{q}^E = \overline{q(x,\, z,\, t)} = \bar{q} \tag{2.6}$$

The Stokes drift associated with the waves is the difference between the GLM and Eulerian mean velocities:

$$\bar{u}^S \equiv \bar{u}^L - \bar{u}^E \tag{2.7}$$

Consider next the instantaneous difference between the horizontal velocity at the displaced minus undisplaced locations:

$$\begin{aligned} u^{IS} &\equiv u(x+\chi, z+\zeta, t) - u(x,z,t) \\ &\approx \{\chi\partial_x u + \zeta\partial_z u\}_{(x,y,t)} + (H.O.) \end{aligned} \tag{2.8}$$

For a monochromatic small amplitude wave in deep water, the velocity field can be written as

$$u(x,z,t) = \mathrm{Re}\{U(x,z,t)\} = \mathrm{Re}\{P_u(k,\sigma)e^{kz}\, e^{i(kx-\sigma t)}\} \tag{2.9}$$

where P_u is a complex velocity amplitude (like a single Fourier component). The horizontal displacement field is a time integral of horizontal velocity:

$$\chi = \int_{t_0}^{t} u\, dt = \mathrm{Re}\{(-i\sigma)^{-1}U\} = -\sigma^{-1}\,\mathrm{Im}\{U\} \tag{2.10}$$

and the vertical displacement field is

$$\zeta = \sigma^{-1}\,\mathrm{Re}\{U\} \tag{2.11}$$

The velocity gradients are

$$\partial_x u = \mathrm{Re}\{(ik)U\} = -k\,\mathrm{Im}\{U\} \quad \text{and} \quad \partial_z u = \mathrm{Re}\{(k)U\} = k\,\mathrm{Re}\{U\} \tag{2.12}$$

To second order in wave steepness, the instantaneous Stokes drift is

$$u^{IS} \approx \{\chi \partial_x u + \zeta \partial_z u\}_{(x,y,t)} = (k/\sigma)\{\mathrm{Im}(U)^2 + \mathrm{Re}(U)^2\} = |U|^2 / c \tag{2.13}$$

Note in particular that half the net Stokes drift comes from the vertical displacements, and half from the horizontal (in deep water). As an aside, a remarkable property of this result is that it is constant with respect to the wave phase; i.e., no averaging is required (for a monochromatic deep-water wave).

The above considers a single wave component. For a spectrum of waves, the nonlinearity of (2.8) or (2.13) means that shorter waves riding on longer ones introduce high-frequency oscillations to $|U|$, so some form of wave-filtering is required. This is addressed in section 5, where methods are developed to use wavenumber-frequency Fourier coefficients to estimate the Stokes drift as well as to implement a wave-filter. Appending to the above aside, it remains true for multiple deep-water waves that half the net Stokes drift comes from vertical and half from horizontal displacements.

Before proceeding with estimates of the time-space characteristics of the Stokes drift, the experimental setting and data collection is described. Then an estimate of the global average Stokes drift used previously is re-examined, leading to detailed consideration of the effects of the wave displacements on the measurements themselves, and also helping to motivate the wavenumber-frequency analysis that follows.

3. Experimental Setting

The data considered here were gathered aboard the R/P FLIP, in conjunction with the Hawaii Ocean Mixing Experiment (HOME; see *Rudnick et al.* [2003]), at a location just WNW of Oahu (figure 1). Typical conditions there consist of steady trade-winds of 10 to 12 m/s from the East, with occasional storms or calm periods. During the data-gathering period, the initially typical winds dropped, remained slack for a few days, and resumed (figure 2). Surface currents are dominated by tides, which cycled from spring- to neap- to spring-tides again. The surface wave field varied from strongly bi-modal (or multi-modal; i.e., distinct wave groups from several directions) to approximately unimodal (a single dominant direction and peak frequency).

A key ingredient in current theories of LC generation is the Stokes drift profile due to surface waves (as noted above). Quantitative estimation of the Stokes drift requires good wave data: direction and frequency must be resolved over a wide range of scales. To provide this, a 50 kHz "Long-Range Phased-Array Doppler Sonar" (LRPADS) was operated continuously for about 20 days, from September 14 to October 5, 2002. This provides both the surface waves and the underlying surface flows over a considerable area, with continuous coverage in both space and time.

The operating principals and concerns for a phased-array Doppler sonar are described in detail in [*Smith*, 2002]. In brief, an acoustic signal is transmitted in a broad horizontal fan, with vertical beam-width sufficient to encounter the surface beginning a few tens of meters away, and continuing until attenuation reduces the backscattered signal level below the ambient noise. The near-surface is a region of strong backscatter. Bubbles, when present, provide backscatter that is of order 10^4 times louder than that from other scatterers. In the absence of bubbles, materials at the surface still often produce a signal stronger than the volume scatter from below. Thus, the backscatter can for the most part be considered to be from the surface. Since the sample volumes are so strongly surface-trapped, acoustic sheltering of wave crests by closer troughs is an aspect to be considered (see section 4). The backscattered signal is received on a linear transducer array and digitally beamformed into an array of angles spanning the breadth of the transmitted fan. Time of flight since transmission is combined with the speed of sound to range-gate the returns into bins spanning the usable range. The bulk of the acoustic paths are below the bubble-layer, so soundspeed variations are small, and a value based on the mean temperature and salinity in the surface mixed layer can be used. The returns are segmented in both range and angle, so each "ping" results in many measurements distributed over a pie-shaped surface area. For the LRPADS as configured in HOME, an area extending roughly 1.5 km in range and 45° in bearing is segmented into measurement bins about 1.3° wide (35 beams) and 7.5 m in range (200 range bins), a total of 7000 locations. The entire area is sampled every 2.5 s (the time needed for sound to propagate out some 1800 m and back) over the whole 20 day period (with few gaps, the largest a few minutes long). The

LRPADS was operated with about 7 kHz usable bandwidth. Repeat-sequence codes [*Pinkel and Smith*, 1992] were used to reduce Doppler noise, using 23-bit Barker codes, resulting in single-ping rms noise levels of about 10 cm/s per range/angle bin. With 7 kHz bandwidth, and 50 kHz center frequency, the individual code bits correspond to about 7 wave cycles each. An acoustic plane wave from the outermost angles, ± 22°, completes 16 cycles across the face of the receive array, corresponding to more than two bits' worth; thus, beamforming must be done via time-delay. On one hand, this is more computationally demanding than simple FFT beamforming; on the other, it reduces the ambiguity between the Nyquist wavenumber angles (+22° and –22°), permitting the beamforming to be extended slightly beyond that limit. As operated, the selectivity between +22° and –22° for the LRPADS in HOME appears empirically to be of order 6 dB. Since computation has become relatively fast and cheap, this is a favorable trade-off (though the processing pushes the limits of the fastest desktop workstations available to date). For convenience in handling, the continuous data stream is segmented into raw data files of order 640 MB size, typically corresponding to 208 pings or about 8.5 minutes worth of data per file. After beamforming and covariance processing [*Rummler*, 1968; *Pinkel and Smith*, 1992], the corresponding size per file is reduced to about 30 MB. Retaining the raw digitized data permits experimentation with new beamforming algorithms, near-field focusing, and/or (of note here) re-sampling with higher range resolution. The inexpensive large-volume data storage available now makes it possible and therefore worthwhile to save raw data, facilitating such further development and refinement of the analysis.

The Doppler shift is estimated with a time-lagged covariance technique [*Rummler*, 1968], where each "ping" is considered independently. With this scheme, there is a finite level of Doppler noise even at high signal-to-noise ratio (*SNR*; see *Theriault* [1986]; *Brumley et al.* [1991]; *Pinkel and Smith* [1992]; *Trevorrow and Farmer* [1992]). At the farthest ranges, the *SNR* decreases as the signal fades into the ambient acoustic noise, further degrading the estimates. For finite *SNR*, use is made of the empirical finding [*Pinkel and Smith*, 1992] that the error variance e_σ^2 of the Doppler shifted frequency estimate is about twice the value of the lower bound given by *Theriault* [1986]:

$$e_\sigma^2 \approx \frac{2}{LT_aT_o}\left(1+\frac{36}{SNR}+\frac{30}{SNR^2}\right) \tag{3.1}$$

where L is the number of independent samples (here, the number of bits in the repeated code), T_o is the duration of the total transmitted code sequence less covariance lag time ("overlap time"), and T_a is the averaging window of the return (see also [*Smith*, 2002]). The measured backscatter intensity is used to estimate the SNR, assuming the farthest ranges contain only noise. To facilitate objective viewing and to pre-condition the data for Fourier analysis, the velocity estimates are scaled to make the net error variance constant with range; i.e., they are divided by the square-root of the portion in parentheses in (3.1). As a consequence, the values at the farthest ranges, where the signal approaches pure noise, are tapered smoothly to zero.

Example single-ping frames from sequences of slope and velocity images are shown in figure 3. The spatial dynamic range of the measurements is illustrated better in the surface slope image: wavelengths from about 15 m to over 1 km are resolved, corresponding to wave periods from 3 to more than 20 seconds, longer than any swell in this data set. The full three-dimensional (2 space +time) evolution of the surface velocity fields can be viewed in the form of movies, or various slices through the 3D data volume or corresponding 3D spectra can be considered.

4. Area-Mean Velocities and Stokes Drift.

The most direct way to estimate the Stokes drift would be to simultaneously measure a Lagrangian and a corresponding Eulerian velocity. Two area-mean velocity estimates can be formed from LRPADS data that tend toward this ideal, but fall short. The two estimates arise from (1) the area-mean displacement of all intensity features from one time to another (for details, see *Smith* [1998]); and (2) weighted averages of the Doppler shifts over the area, yielding mean along-axis (cosine-weighted) and across-axis (sine-weighted) velocity components (where the "axis" is the center angle of the beamformed array). The first, based on an area-mean feature-tracking algorithm, is a Lagrangian velocity estimate. The other, based on mean Doppler shifts, is not exactly Eulerian or Lagrangian, but something between. This requires further analysis to understand, and a few assumptions to evaluate quantitatively. The detailed examination (below) leads to another more accurate way to estimate

Stokes drift and other effects. Nevertheless, the difference between the two area-mean velocities is a reasonable approximation of the Stokes drift, within 25%, as will be seen. This area-mean approach is "method 1" for the estimation of Stokes drift.

Development of this approach arose from an unrelated motivation: simple time-averaging to eliminate surface waves can lead to significant smearing of features due to advection by the mean flow. To counter this, a method was developed to form averages that move along with the features (e.g., irregular bubble clouds), making use of an area-mean feature-tracking algorithm (for details, see [*Smith*, 1998]). A fringe benefit is the Lagrangian estimate of the area-mean horizontal velocity (figure 4). An alternative is to form averages moving with the mean derived from the Doppler signal (see above); however, the two differ systematically, and the former maintains sharper features. *Smith* [1998] noted that this difference corresponds closely to the Stokes drift calculated from a resistance wire (surface elevation) array. The same feature-tracking algorithm was applied to the HOME LRPADS data set, and figure 5 shows a comparison of the feature-track/Doppler velocity difference (henceforth "FDV") versus a "rule-of-thumb" estimate that the Stokes drift is 1 to 2% of the windspeed. The best match is found for 1.25% W_{10}, which is within the expected range. It is also seen that the difference vector is roughly parallel to the wind. As an aside, note that while the overall agreement on longer time scales between the FDV and 1.25% W_{10} is quite close, the two vary out of phase with approximately the tidal frequency over the later windy period (year-days 272 to 276). This suggests that the waves respond to the large-scale currents associated with the tides in addition to the local wind. Investigation of this is suggested for future work.

Both measurements can be understood as vertical as well as horizontal averages, with the vertical averaging determined by the vertical bubble (dominant scatterers) distribution. The feature-tracking velocities are estimates of the mean bubble advection. Since the bubbles are embedded in the fluid, and the macroscopic evolution of bubble clouds is slow compared to the time needed to resolve advection (10 to 30 s), the result is essentially an average over both the surface area observed and the bubble depth distribution. The Doppler estimates are also weighted in the vertical by the bubble-cloud depth dependence; however, they may also be affected by sheltering of wave crests, as acoustic rays must pass under the preceding wave troughs.

The detailed behavior of the Doppler means depends on the incident angle of the sound on the surface. For sound incident from below at angles steeper than the wave slopes, the measurement volume rises and falls with the bubble-clouds, but has fixed range bounds; i.e., without sheltering the Doppler measurement effectively moves in the vertical but not horizontally. As noted in section 2, half the Stokes drift comes from vertical displacements, and half comes from horizontal, so in this case the difference between feature-track and Doppler velocities (FDV) should correspond to half the Stokes drift (since the former includes it in full and the latter only by half, as noted by *Smith* [1992]). In contrast, at grazing angles wave troughs shelter more distant wave crests, limiting the acoustic backscatter measurement volume to a more nearly fixed depth interval below the typical wave trough depth (see figure 6). This helps explain the later finding, made with a shallower deployment of the sonar system, that the difference approaches the full value of the Stokes drift rather than just half [*Smith*, 1998]: With a typical wave steepness of 0.1 and a sonar deployment at 35 m depth (as in the 1990 deployment reported in [*Smith*, 1992]), the former behavior would be expected out to about 350 m range (nearly full range in that case). With a sonar deployment at 15 m depth, as in the latter (1995) deployment, some sheltering of crests would be expected beyond 150 m; focusing on ranges from 200 to 450 m, sheltering is expected in that case.

To examine the effects of acoustic sheltering of wave crests, and the transition between the two limiting behaviors, simulations were performed. Effects of the sheltering on both wave orbital velocities and on a background surface shear layer are considered. Sheltering is determined by a simple algorithm, considering a single sonar beam in isolation, and assuming the acoustic rays are straight (although the bubbles affect soundspeed and hence cause refraction, the distances from troughs to crests are too short for the rays to refract significantly, so this approximation is reasonable). First a wave elevation profile $\zeta(r,t)$ is defined as a function of range and time, in a form similar to that of the velocity data. To illuminate effects of wave groups, at least two wave components are required. For each synthetic ping, the array of vertical angles from the sonar to the center of each range bin is defined via it's sine, which is the ratio of (ζ + sonar depth) to the radial distance to the center of the range bin. Then, starting from zero range and working outwards, the minimum value of all previous sine-angles out to the target range is retained. By induction, this requires merely taking the minimum of the current and previous value as one works outward (figure 6). The resulting "sheltered depths" z_S can be used to determine either the distance below the true surface ("sheltering thickness") or the distance above or below a fixed reference depth for this upper boundary of the volume sampled acoustically. The mean velocity calculated at the moving surface, at a fixed level (near a typical trough depth, say), and at the simulated sheltered depths in between can be directly compared (figure 7). The sheltered depth always lies between the actual surface and the depth of the wave troughs; thus the result lies between a surface-tracking semi-Lagrangian estimate and an Eulerian estimate at the depth of a typical wave trough. The simulations show how measured values should differ from surface-following versus fixed-depth values as a function of range: the Doppler measurement (black line, figure 7) matches the surface-tracking value (upper line, figure 7) over the first 150 m, and then moves gradually toward the fixed-depth value (*x*-axis, figure 7) at the most distant ranges, as anticipated. The transition is not quick. For the wave steepness and sonar depth as simulated, the transition is only 50% complete at 600 m range. Using estimates averaged over a middle segment (say 300 to 1200 m), the difference between the Doppler mean and feature-tracking velocities is expected to be about 75% of the Stokes drift. The ability to distinguish this from 100% in the presence of background variability is dubious, since the Stokes drift could be anywhere between about 1 to 2% of the windspeed. Because wave steepness is robust, however, the "calibration coefficient" between the FDV and true Stokes drift should remain roughly constant for a given deployment geometry.

The measured Doppler shift in each range/angle bin is effectively a bubble-weighted mean velocity. In the ocean, bubble density generally decreases exponentially below the surface, with a depth scale (depending weakly on wind speed) of order 1.5 m for 10 m/s winds [*Thorpe*, 1986; *Crawford and Farmer*, 1987]. A reasonable model for the bubble distribution is

$$B \approx B(x,y,t)\, e^{k_b z} \tag{4.1}$$

where $B(x,y,t)$ can vary over several orders of magnitude [*Crawford and Farmer*, 1987], but the depth scale $k_b \approx (1.5\text{ m})^{-1}$ is assumed not to vary spatially. The bubble-weighted depth average of a quantity "$q(z)$" is formed from the sheltered depth downwards:

$$\overline{q}^{z} = \frac{\int_{-\infty}^{z_s} q\, e^{k_b z}\, dz}{\int_{-\infty}^{z_s} e^{k_b z}\, dz} = k_b e^{-k_b z_s} \int_{-\infty}^{z_s} q\, e^{k_b z}\, dz. \tag{4.2}$$

A surface wave of frequency *f* and corresponding wavenumber k_f yields a response of the form

$$\overline{u(r,t)}^{z} = U_0 \cos(\theta_k - \theta_r) e^{i(k_r r - 2\pi f t)} \frac{k_b}{k_b + k_f} e^{k_f z_s} = u_r(r,t) \left(\frac{e^{k_f z_s}}{1 + k_f / k_b} \right) \tag{4.3}$$

where the nominal radial current u_r is defined at the mean surface, $z = 0$. The final response factor (in parentheses) can be used to adjust the measured velocities to estimate what the value would be at $z = 0$ or $z = \zeta$. Near the high-*k* cutoff, where $k_f \approx 0.39$ rad/m, the denominator is about 1.6. The denominator is a fixed correction that can be performed simply in the frequency domain (using linear dispersion to get k_f); this correction is henceforth taken as applied, and the term is dropped from explicit analysis. The remainder of the effect lies in the placement of the starting depth of the average, the sheltered depth z_s. Each wave component has a different depth-scale *k*, while the sheltered depths are defined over the time-space domain from the entire ensemble of waves; thus, compensating for this in the data requires the equivalent of a “slow” Fourier transform. This is discussed further in section 5.

Presence of a thin wind-drift layer also affects the results with crest sheltering. For simplicity, consider a steady wind-drift layer with an exponential drift profile with scale-depth k_d^{-1}. As described in *Smith* [1986], the overall character of the wind-drift layer is well captured by this approximate form, and the results are easily manipulated and understood. Modulation of the wind-drift by the waves is neglected, as this is expected to be small except very near breaking [*Longuet-Higgins*, 1969a; *Banner and Phillips*, 1974; *Smith*, 1986]. Then the weighted-average response 4.3 applies, with k_d substituted for k_f. Given the wind-drift strength and depth-scale, the effect can be efficiently calculated and accounted for. A reasonable estimate of the surface wind-drift is 1.6% W_{10}, where W_{10} is the windspeed at 10 m height [*Wu*, 1975; *Plant and Wright*, 1980]. For molecular viscosity, the layer would be only a few mm thick, and 4.3 shows its bubble-weighted average would be negligible. On the other hand, an average wave-breaking induced eddy-viscosity [cf. *Terray et al.*, 1996] would result in a depth-scale comparable to the rms wave amplitude. In simulations, the greatest effect occurs for a wind-drift depth-scale between the rms sheltering thickness and the averaging (bubble depth) scale. The latter scale (rms amplitude) is in this range, so its use is unlikely to result in an underestimate of the effects. From simulations, the two main effects are (1) a decrease in the mean downwind flow in proportion to sheltering; and (2) a systematic decrease in the measured orbital velocities with sheltering, as the forward velocity in each crest is decreased by the amount of missing wind-drift there. The former produces an increase in the predicted FDV, since the missing drift only affects the Doppler measurement, and so helps explain the tendency toward the full value of Stokes drift found in the observations. The latter helps explain a systematic decrease in wave amplitude with range (although finite angular spreading of the beams has a similar effect due to cross-beam smoothing of wave motion). Other effects of clipping the wind-drift layer, which appear at wave harmonics and at group-envelope scales, are small enough to neglect.

Sheltering can be estimated for the actual data, using the same minimum-angle algorithm described above (figure 8). The method used for estimating elevation from time-range segments of radial velocity is outlined in section 5. In the data segments shown here, the sheltering thickness increases to 0.5 to 1 m at the greatest ranges, which is only slightly smaller than k_b^{-1}. For the wind-drift parameters used here (depth-scale 1 m, surface value 16 cm/s), estimated drift anomalies are roughly proportional to the sheltering thickness, with maxima near 15 cm/s (see figure 8, but imagine the scale is 0 to 15 cm/s). Figure 9 shows the time-mean drift anomaly from the same data (and wind-drift magnitude and depth-scale). Assuming an area mean can be substituted for a time-mean (and vice-versus), this would correspond to an increased FDV estimate as well. Since the wind-drift deficit amounts to about 1/6 of the Stokes drift in magnitude, this would bring the FDV value (formed over 200 to 1100 m in range) up from 75% to about 92% of the Stokes drift. Finally, the estimated leakage into group-envelope characteristics and into higher harmonics of the waves is small, as anticipated from the simulations. This ordering of effects is corroborated by the backscatter intensity data, which acts mathematically like a proxy for a wind-drift-layer (though with a different depth-scale): as the exponentially surface-trapped bubbles are moved up and down into sheltered regions, the resulting modulation of the intensity signal is strong along the surface wave dispersion part of the corresponding k–f spectrum, but almost undetectable along the 5 m/s propagation line corresponding to group-envelope characteristics (see figure 11, left panel).

The explicit extrapolation of wave-motion from sheltered depths to both the moving surface and a fixed level provides an alternative way to evaluate the Stokes drift: the difference between the two is half the drift. In addition, this approach provides objective estimates of the Eulerian velocity fields. This is developed below (section 5) as method 3.

5. Stokes Drift Estimates Using Frequency-Wavenumber Spectra

In this section, estimation of time-space maps of the radial component of Stokes drift along a given sonar beam direction is considered. The objective is to produce estimates of the Stokes drift that are directly analogous to the radial velocity measurements of the underlying flow for each beam. Then time-range propagation characteristics of the Stokes drift can be examined to see (1) how intermittent the wave influence or interaction might be; and (2) how it compares to the observed underlying flow. Two methods are developed, using frequency-wavenumber Fourier coefficients formed from time-range data slices.

A natural and useful slice through the 3D time-space data volume is a time-range plot, formed along a single direction. Because the heading of FLIP, and hence of the array, can vary by tens of degrees over timescales of minutes, the beamformed data are first interpolated onto a set of fixed directions. Time–range plots reveal both phase propagation and group (envelope) characteristics of surface waves along a given direction. For example, figure 10 shows a time-range plot for a beam directed roughly downwind. Compact packets of roughly 7 s period waves can be seen, forming slashes at an angle on the time-range plane corresponding to about 5 m/s (the group velocity for 7 s waves, which also have a phase velocity near the windspeed, 10 m/s). These compact packets are distinct from the spectral peak waves (near 10.6 s), which form broader groups (e.g., in figure 10 note a longer group starting at 300 s and propagating upward at a steeper angle, near 7.5 m/s, reaching 1000 m at about 435 s).

Figure 11 shows the log-magnitude of the 2D Fourier transform of the data shown in figure 10, color-contoured on the k-f plane. Since the data are real, the $(+f, +k_r)$ components are redundant with respect to the conjugate $(-f, -k_r)$ components. The wavenumbers are shifted so that $k_r = 0$ is centered, but the frequencies are left un-shifted so the variance for frequencies past the Nyquist frequency, which are aliased onto negative frequencies, aligns with the un-aliased variance along the surface wave dispersion curve. The continuity of variance along the dispersion curve suggests this aliased information can be used. Because of the external knowledge that the waves propagate predominantly downwind, the ambiguity of location on the aliased *k-f* plane can be resolved. As seen in figure 11, the resolved (but aliased) surface wave variance extends well past the frequency Nyquist limit, f_N = 0.2 Hz, to more than 0.3 Hz. The downwind surface wave dispersion branch also extends beyond the original Nyquist wavenumber k_N = 0.047 cycles/m to beyond 0.06 cycles/m. Resolving this alias is important not only in effectively enhancing resolution of the surface wave measurements, but also because this second alias of the wave variance would otherwise be falsely identified as slower-moving "non-wave" activity (see figure 11, green alias delimiters). After masking (zero-filling) to remove the redundant or aliased information, the remaining *k-f* Fourier coefficients are interpreted with the convention of time going forward and waves propagating in the same direction as **k**; i.e., the ($+f$, $\pm k_r$) half plane is retained, and the amplitudes are adjusted to preserve the net variance. To resolve the unwrapped wave information, the FFT size is doubled in the *f* direction and increased by 1.5 in the *k*-direction. The inverse Fourier transform thus has results interpolated to twice the sample rate (samples every 1.25 s rather than 2.5 s) and 2/3 the range-bin size (7.1 m bins rather than 10.6 m).

A better solution to the wavenumber aliasing is to re-analyze the raw data with finer range resolution. Reducing the range-bin size to 7.5 m increases the Nyquist wavenumber to 0.065 cycles/m, sufficient to keep the resolved surface wave variance from wrapping into the slower-moving "non-wave" area of the spectrum (figure 12). While the error variance of each estimate is increased, the increase is in proportion to the increase in area on the *k*-axis; i.e., the spectral noise floor remains the same. Henceforth the re-sampled higher-resolution data are used.

Linear Dispersion and Spectral Bounds

The *k-f* spectra strongly favor waves propagating directly along the beam. This is largely because of the cosine response of the measured along-beam velocity component to propagating waves. On the *k-f* plane, the linear dispersion curve is $k_r \approx k_f$, where k_f is the magnitude of the wavenumber for a given frequency *f*. In deep water, and including advection by a mean velocity *U*, linear dispersion yields (note conversion from Hz to rad/s):

$$\sigma = 2\pi f = (g k_f)^{1/2} + U k_f \cos(\theta_k - \theta_u) \tag{5.1}$$

where $\theta_k - \theta_u$ is the angle between the wavenumber and the mean flow directions. This can be inverted into a form that is stable with respect to $U \to 0$ (substitute $x = k_f^{-1/2}$):

$$k_f = \left[\frac{2\sigma g^{-1/2}}{1 + [1 + 4U\sigma g^{-1} \cos(\theta_k - \theta_u)]^{1/2}} \right]^2 \tag{5.2}$$

(*Smith and Bullard* [1995], equation 5.2; however, note their equation 5.1 is erroneous). At higher wavenumbers advection becomes more noticeable on two counts: first, the fractional change in *k* at fixed *f* and *U* is larger due to the decreasing phase speed (so $U\sigma g^{-1}$ is larger); and second, for a larger value of *k* the spectral resolution is a smaller fraction of *k*. Thus, at the high end resolved here (near 3 s period) velocities of even a few cm/s make a detectable difference. Note also that the advection velocity of the shorter waves includes the Stokes drift of the longer waves; at the level of accuracy required here, this can be parameterized as 1.25% W_{10} (wind at 10 m height), which is added to the Doppler mean estimate (see figure 4).

Surface waves are both the fastest moving and the largest amplitude signal detected. To delimit the area on the *k*-*f* plane dominated by waves, objective bounds on k_r vs. *f* are determined based on a balance between wave variance and the noise floor of the measurement. Dimensional analysis, assuming all but gravity to be small influences, yields an “equilibrium spectrum” for surface orbital velocity variance of the form

$$P_u^2(f) \propto f^{-1}(g/f)^2 \propto f^{-3} \tag{5.3}$$

On the *k*-*f* plane this variance is spread out from $k_r = 0$ to $k_r = k_f \propto f^2$, so that

$$P_u^2(f,k) \propto f^{-5}, \quad -k_f < k_r < +k_f \tag{5.4}$$

The cosine-response of the radial current measurement results in a further k_r dependence, yielding

$$P_u^2(f,k_r) = P_u^2(f) k_f^{-1} \cos^2(\theta_k - \theta_r) \propto f^{-5}\left(k_r/k_f\right)^2 \propto f^{-9} k_r^2 \tag{5.5}$$

Thus the bound is set according to

$$k_{low} \equiv k_r(lowerbound) \propto f^{-4.5} \tag{5.6}$$

To set the constant for this limit, the curve is made to intersect the linear dispersion curve where the latter fades into the noise. For example, in figures 11 and 12, $k_{low} = k_f$ is enforced at $k_{tr} = 0.065$ cycles/m, with the corresponding frequency $f_{tr} \approx 0.33$ Hz.

The upper bound must be above the dispersion curve due to finite spectral leakage. The upper limit is not as critical as the lower because (1) the variance there is primarily spectral leakage, and (2) adjustments to be applied that involve dividing by $\cos(\theta_k - \theta_r)$, for example (see below), are not singular there. Here the upper limit is set assuming (typical) spectral leakage of the form

$$P(k_f + \Delta k) \propto f(\Delta k) \to \Delta k^{-n} \tag{5.7}$$

where the limit is approached quickly; i.e. for Δk more than a few times the spectral resolution. To form a simple parametric curve describing the total energy at f, we assume $P_u^{\,2}$ approaches an f^{-3} decay at high frequency (as before), is maximal at some specified frequency f_0, and rolls off to zero for small f even faster, say as f^{6}. Allowing for leakage behavior as in 5.7 with n = 2, and adding this to dispersion, a curve of the form

$$k_{hi} = k_f + \frac{2D_0}{(f/f_0)^{3/2} + (f/f_0)^{-3}} \tag{5.8}$$

is adopted, where D_0 is a specified maximal distance above the dispersion curve, achieved at $f = f_0$. For example, in figure 11, the values D_0 = 12(Δk) and f_0 = 0.1 Hz were used, where Δk is now re-defined as the spectral k- interval for the finite FFT employed (≈ 1 cycle per 2.7 km). Finally, a small amount (Δk) is subtracted to permit more low-frequency/low-wavenumber variance to pass, since surface waves longer than 30 s or so are not seen in this data set, and some of the "5 m/s variance" crosses the axis at small but finite fequencies. (see figures 11, 12).

Stokes drift from LRPADS radial velocity data.

Estimation of the radial (along-beam) component of Stokes drift along individual beams of the LRPADS data can now be addressed. Waves propagating at right angles to the beam contribute nothing to the net along-beam drift, so it is unimportant that the measurements from the beam are insensitive to such waves. The results from all the beams can be combined so the full space-time evolution of the Stokes drift can be evaluated, and time-space maps of the radial Stokes drift can be directly compared to the underlying "non-wave" flow measured simultaneously.

The two methods developed here work from the 2D k–f Fourier coefficients. Zero-padding the negative frequencies and doing the inverse transform results in both the (oversampled) original timeseries (real part of the result) and a constructed out-of-phase part (or Hilbert transform; imaginary part). For a narrow-band process, the absolute value corresponds to the envelope of the radial component of velocity

$$|u_r(r,t)|^2 = |u|^2 \cos^2(\theta_k - \theta_r) \qquad (5.9)$$

whereas the radial component of Stokes drift

$$u_r^S(r,t) = u^S(r,t)\cos(\theta_k - \theta_r) = c^{-1}|u|^2 \cos(\theta_k - \theta_r) \qquad (5.10)$$

is the quantity of interest. The phase speed c is a simple function of frequency; from dispersion

$$c \equiv \sigma / k_f = 2\pi f / k_f \qquad (5.11)$$

The more challenging part is to account for the angular response: to reduced from $\cos^2$ to cos requires dividing by (k_r/k_f), which is singular at $k_r = 0$. The objectively derived low-k cutoff (5.6) provides the necessary tool. Rather than truncate sharply at k_{low}, an arbitrary but smoothly weighted function is employed, of the form

$$W(k_r, f) = \left(\frac{x^3}{1+x^4}\right)\left(\frac{k_f}{k_{low}}\right), \quad \text{where} \quad x \equiv \frac{k_r}{k_{low}(f)} \tag{5.12}$$

and k_{low} is as defined above (5.6). This has the desirable properties that it: (1) $\to 0$ rapidly as $k_r \to 0$; (2) $\to (\cos(\theta_k - \theta_r))^{-1}$ rapidly for $k_r > k_{low}$; (3) decreases smoothly through the threshold value k_r = k_{low}.; and (4) changes sign with k_r, as it should.

One way to obtain estimates of the Stokes drift is to weight the Fourier coefficients by the square-root of the net conversion factor:

$$P_u(k_r, f) \to P_u(k_r, f)\big(W(k_r, f)/c(f)\big)^{1/2} \tag{5.13}$$

This, when reverse-transformed, yields a "root-velocity" field whose absolute value squared is (nominally) the Stokes drift (this is "method 2"). However, note that the sign of k_r is important: the Stokes velocity from incoming waves is in the opposite direction from those that are outgoing. The weighting function W also changes sign, but here there is the potential to erroneously take the square root of (–1), rather than get the right result. However, since the transforms are complex, and absolute values eventually taken, any change in sign is effectively ignored. The simplest fix is to treat the $+k_r$ and $-k_r$ parts separately. Here the upwind-directed portion is so weak that only the downwind portion need be treated. Method 2 has the advantage of speed, since it employs only FFT operations and a weighting; yet it provides more detailed time-space information than method 1, the area-mean FDV.

Another approach is to take advantage of the fact that for deep water waves the vertical displacements alone can be used to estimate half the difference between the Lagrangian and Eulerian velocities ("method 3," as indicated in sections 2 and 4). To this end, the velocity fields are extrapolated vertically from the measurement level to both a constant level (e.g. z = 0) and to the moving surface (at $z = \zeta$). Method 3 has the advantages of (a) explicitly considering the sheltering of crests; (b) properly handling upwind versus downwind directed components; and (c) providing objective estimates of the Eulerian and semi-Lagrangian flows, corrected for sheltering effects. However, it is computationally more demanding.

Elevation displacements ζ are needed both to evaluate sheltering and to implement method 3. These are to be estimated from the radial component of horizontal velocity, which is insensitive to waves propagating at right angles to the beam. To control singularities in this estimate, we use

$$\zeta = \left(\frac{\sigma^{-1} u_r}{\cos(\theta_k - \theta_r)} \right) \approx \sigma^{-1} u_r \; W(k_r, \sigma), \tag{5.14}$$

where W is the inverse-cosine weighting function with built-in cutoff defined above (5.12). Since both the radial Stokes drift and the sheltering effects are also insensitive to the perpendicularly propagating waves, the loss of information about them is ultimately not important.

The estimated elevations are used to explicitly calculate displaced and fixed-level radial velocities, frequency by frequency:

$$u_r^{\zeta}(r,t,f) \approx \{P_u(r,f)\, e^{-i(2\pi f)t}\}\, e^{k_f(\zeta - z_m)} \tag{5.15}$$

and

$$u_r^{0}(r,t,f) \approx \{P_u(r,f)\, e^{-i(2\pi f)t}\}\, e^{-k_f z_m} \tag{5.16}$$

where z_m is the measurement depth (the "sheltered depth" discussed in section 4), both z_m and ζ are functions of range and time, and the subscript r denotes the radial (along-beam) component of velocity. Note that the total displacement fields $z_m(r,t)$ and $\zeta(r,t)$ are used for all frequencies; this makes the method 3 result fundamentally different from method 2. The portion inside braces {} is understood as an inverse Fourier operation carried out on a single frequency component (there may be an additional normalization factor, depending on the Fourier transform definition used). The results are then integrated over f at each location in range-time space (or, for discretely sampled finite-length data, summed) to yield the net displaced (semi-Lagrangian) and fixed-level (Eulerian) radial component of the velocity fields. The wave-averaged difference between the vertically displaced and fixed-level velocities is half the Stokes drift, so the estimate by method 3 is

$$u_r^S(r,t) \approx 2\left\langle u_r^\zeta - u_r^0 \right\rangle \tag{5.17}$$

where < > denotes an average over the waves. Here the *k-f* plane separation described above is used to separate wave-like and non-wave variance. Note in particular that the 5 m/s ridge extends far enough in both *f* and *k* that a simple time filter would be insufficient to separate it from the waves. Extensive combined space and time information is required to detect this phenomenon.

Results of the displacement (eq. 5.17) versus the root-velocity (eq. 5.13) methods (2 and 3) for estimating the Stokes drift are close but not identical. Figure 13 shows a comparison between the time-mean Stokes drift estimates via the two methods versus range over the same data segment as shown in figure 10. The agreement is good, verifying that the upwind-directed waves are negligible and that the narrow-band assumption is a weak requirement. Both methods lead to Stokes drift estimates that weaken with range. The estimated effect of a nominal wind-drift layer (cf. section 4) was incorporated (which does help flatten this response profile slightly), but there remains lateral averaging as the beams spread. The enhanced range sampling of 7.5 m matches the beam width near 330 m range. Beyond this range the cross-beam smoothing dominates, and waves at any finite angle to the beam experience progressively more suppression. An adjustment by a statistically derived "transfer coefficient" T_C is also shown; this is discussed in section 6, below.

Figure 14 shows a time-range plot of the radial Stokes drift for the same time segment and beam as in figure 10, using the displacement method (5.17). The results clearly show wave groups, as expected. Note particularly the correspondence between the strongest Stokes-drift signals and the compact higher-frequency groups propagating at roughly 5 m/s seen in figure 10.

For a spectrum of the form posited above, the net contribution to Stokes drift as a function of frequency drops off weakly:

$$u^S(f) \approx P_u^2(f)(2\pi f/g) \propto f^{-2} \tag{5.18}$$

The high-frequency tail of the spectrum affects the Stokes drift at the actual surface. This can be addressed by parameterization in terms of a local equilibrium with the wind (e.g., as in [*Hara and Belcher*, 2002]), or by using higher-frequency unidirectional data (e.g., from an elevation resistance wire) combined with an assumption that the high-frequency waves propagate downwind with some approximately known directional spread. However, in the context of the forcing of LC or the evolution of bubble clouds, an average over some small but finite depth (say, that of the bubble clouds) is more dynamically relevant. An exponential average of the Stokes drift over $k_b \approx (1.5\text{ m})^{-1}$ results in an effective spectral cutoff near $k_f = k_b/2 \approx (3\text{ m})^{-1}$ (in radians), corresponding to a linear wave of frequency $f \approx 0.3$ Hz. Thus it appears (coincidentally) that the enhanced effective resolution of the de-aliased spectra is adequate to resolve the important part of the wave spectrum and hence of the resulting Stokes drift.

6. Observed Response to Wave Groups.

The next most prominent feature after the surface waves in the *k*–*f* spectra of velocity is a roughly linear ridge along a line near 45° (in figures 11, 12), corresponding to about 5 m/s propagation speed. To see what form this activity takes in the time-space domain, a speed-based filter was applied in *k-f* space, passing variance moving between 4.5 and 6.5 m/s, which was then inverse-transformed. Figure 15 shows two spatial frames from the resulting sequence, 20 s apart (results from all beams, each processed independently). The features associated with this 5 m/s ridge are very narrow in the along-wind direction, but extend coherently a considerable distance in the cross-wind direction. They consist of blue-shift anomalies (i.e., bands of upwind-directed velocity) that propagate downwind.

Figure 16 shows a time-range plot of the wave-filtered Eulerian velocity $U_0(r,t)$. The objective *k-f* bounds (5.6 and 5.8), shown in figure 12 (red lines), were used to exclude the waves, and the results inverse-transformed back to time and range. Of particular note is that blue slashes in figure 16 resemble the red slashes in the Stokes-drift plot (figure 14). In fact, the sum of the two, $U_0 + U_S$, yields a field of velocity that is nearly free of bias in propagation direction (figure 17). This is verified by comparison of the k–f spectra of the Eulerian (U_0) versus the net Lagrangian ($U_0 + U_S$) velocities (figure 18). The spectrum of the wave-filtered Lagrangian velocity has almost no hint of variance (other than noise) along the 5 m/s line, while the Eulerian estimated field has a distinct ridge there.

The wave-filtered Eulerian velocity field is correlated with the Stokes drift at a statistically significant level (figure 19). With N = 208 samples (the number of pings over which the correlations are averaged), the coherence confidence level is [*Thompson*, 1979]

$$C_\alpha^2 \approx 1 - \alpha^{1/(N-1)} = 1 - 0.05^{(1/207)} \approx (0.12)^2 \tag{6.1}$$

where α is the allowed probability of error (α = 0.05 for 95% confidence). The correlation is several times larger than this level (0.3 to 0.4), so robust statistical estimates of the transfer function from Stokes drift to the Eulerian anomaly can be made:

$$T_c = -\left\langle U_S\, U_0 \right\rangle \Big/ \left\langle U_S^2 \right\rangle \tag{6.2}$$

(figure 20; note minus sign here). The Eulerian response is negatively correlated with the Stokes drift, with a transfer coefficient of about 1, indicating that the correlated parts roughly cancel each other out. In fact, it appears necessary to increase the estimated Stokes drift just slightly to achieve complete cancellation. Given the smoothing characteristics of the measurement, such slight underestimation of the Stokes drift is understandable. Also, because the Stokes drift estimates involve squared data while the response estimate does not, such smoothing has a larger effect on the former than the latter.

A linear fit to T_C over the range interval 200 – 1000 m is also shown. Interestingly, application of this linear fit to the Stokes drift estimates makes them vary less with range, without changing the near-range value (figure 7, upper curves). This suggests that the measurement sensitivity decreases with range, but still captures the essential characteristics of the Stokes drift. It also suggests that the cancellation of U_S by U_0 is complete.

The fact that the “5 m/s variance” disappears with the transform to the estimated Lagrangian mean flow is convincing evidence that the Eulerian response is equal and opposite to the Stokes drift (in the near-surface layer sampled). It is difficult to imagine any procedure that could lead coincidentally to such nearly perfect cancellation. Many other data segments have been examined (e.g., figure 15 is from a different segment); in every case this cancellation of Stokes drift and Eulerian flow at the surface takes place.

7. Discussion: Wave Groups and the Expected Response.

Larger scale motion forced by advancing groups of surface waves was discussed in some detail by *Longuet-Higgins and Stewart* [1962, 1964]. While much of the interest centered on intermediate to shallow-water cases, the results have a sensible deep-water limit. To review the deep-water case briefly and simply, *Garrett*'s [1976] formulation is used, in which the wave effects appear as a "wave force" in the momentum equation and a "mass source" at the surface. Consider waves aligned with the *x*-axis, having wavenumber k, and a regular group modulation with wavenumber K (e.g., for the simplest case of two wavenumbers k_1 and k_2, let $k = (k_1+k_2)/2$ and $K = (k_2-k_1)$). Let U be the surface value of the current associated with the induced motion. The near-surface momentum equation is

$$\partial_t U + \partial_x (U^2) + g\partial_x \bar{\zeta} = \rho^{-1} F^W \tag{7.1}$$

where $\bar{\zeta}$ is the surface deflection associated with the response, ρ the water density (assumed constant and set to one), and the wave force F^W is

$$\vec{F}^W \equiv B\vec{M}^W + \vec{M}^W \times (\vec{\nabla} \times \vec{U}) - \vec{U}\left(\vec{\nabla} \bullet \vec{M}^W\right) \tag{7.2}$$

(*Garrett* [1976]; for a finite-depth extension of this see *Smith* [1990]). Here, $\vec{M}^W = \rho T^S$ is the wave momentum. In the first term, B represents a dissipation rate (e.g. by breaking). The second term is the return force resulting from refraction of the waves by the current, and the last accounts for mass transferred from the wave transport to the mean transport at speed U. Here U is assumed small, as is $U^S=2kT^S$, and second order terms are neglected (the second term in 7.1 and the last in 7.2). Breaking and vorticity are also neglected, so in this case the whole wave force is negligible. Under the same assumptions, the surface boundary condition is

$$\partial_t \bar{\zeta} - W = -\partial_x T^S \tag{7.3}$$

where W is the vertical velocity associated with the response (forced long wave). For a wave group with envelope-wavenumber K propagating with group-speed c_g as contemplated here, ∂_t can be replaced by $-c_g \partial_x$ and the response should have a depth dependence of the form e^{Kz} (assuming, as seems reasonable, that the response is irrotational). By continuity, then, W can be replaced by $\partial_x (U/K)$. The momentum and the surface boundary condition reduce to

$$\partial_x \left(-c_g U + g\bar{\zeta} \right) = 0 \tag{7.4}$$

and

$$\partial_x \left(U/K - c_g \bar{\zeta} + T^S \right) = 0 \tag{7.5}$$

respectively. Choosing constants of integration so that U = 0 when $\bar{\zeta}$ = 0, the results have the same form but with the partials dropped. The solution is

$$\bar{\zeta} = (c_g/g)U \tag{7.6}$$

$$U = -\frac{gT^S}{g/K - c_g^2} \tag{7.7}$$

For deep water waves, $c_g^2 = (\frac{1}{2}c)^2 = \frac{1}{4}(g/k)$; using also $T^S = (2k)^{-1} U^S$, 7.7 can be written

$$U = -U^S \left(\frac{2c_g^2}{g/K - c_g^2} \right) = -U^S \left(\frac{(K/2k)}{1-(K/4k)} \right) \tag{7.8}$$

which is useful for comparison with the results of section 6. For compact groups, i.e., as K decreases toward k, the factor in 7.8 increases toward 2/3; but the estimated response U never quite equals $-U^S$ as observed.

This simple analysis has several weaknesses. The separation of scales used to derive these equations becomes invalid as this limit is approached. However, historically such simple 2-scale analyses have proved surprisingly robust, perhaps because of the fundamental footing on conservation of mass and momentum. They generally provide guidance on qualitative behavior of the system, even near the limits of validity. Also, analysis is truncated at second order, whereas the waves at mid-group may be steep; this relates (in extreme form) to the effect of breaking, parameterized as "BM^W" in (7.2). Systematic breaking at the wave-group maxima would have two effects: (1) the resultant wave force opposes the prior response velocity, so it would work to reduce the energy of the response; (2) its integral is out of phase with the prior response, so it would alter the phase.

The observations are dominated by variance along the 5 m/s spectral ridge. Substituting this speed for c_g in equation 7.8, it can be seen that the resulting K-dependence is an approximately linear increase with K. As seen in the k-f spectrum of Eulerian and Lagrangian velocity fields, however (figure 18), there is no evidence of K-dependence in the observed response. Rather, the Eulerian and Stokes drift fields appear to cancel at a one-to-one ratio across all the wavenumbers along the 5 m/s ridge (except perhaps at the lowest wavenumbers). Mismatches at the lowest wavenumbers are not reliable because the mean flow along each beam is underdetermined. The wave-induced motion of FLIP is removed via a full-field average, depending therefore on the ratio of the group-scale to the field of view (approximately 1 km). Spectral leakage from the imperfectly determined means is a concern out to wavenumbers of order 0.005 cycles/m (because the wave variance is so large).

As noted in the introduction, Eulerian counter-flows have also been observed in laboratory experiments (e.g., *Klopman* 1994, as referenced in [*Groeneweg and Klopman*, 1998]; also *Kemp and Simons* [1982, 1983]; *Swan* [1990]; *Jiang and Street* [1991]; *Monismith et al.* [1996]; and others). The treatment of *Groeneweg and Klopman* [1998] is based on a WKBJ-type asymptotic expansion, so separation of scales is still a requirement; however, the laboratory results pertain with statistically steady waves and flows, so the "group size" is infinite. Although they do not explicitly make this comparison, the change in profile from case to case (no waves, down-current waves, up-current waves) is approximately equal to the Stokes drift profile calculated from the wave parameters as given. Because of the complexity of their numerical model, it is difficult to pinpoint where it differs from the above simplified exposition, and hence how the difference in predicted scale of the response arises. One possibility is that, because they treat the full problem including viscosity and turbulence, their approach and solution permits vorticity in the (steady) response. In any case, both the analysis of *Groeneweg and Klopman* [1998] and the observations presented here suggest that the balance between the Stokes drift and Eulerian counter-flow may be a more general result, applicable outside the laboratory.

8. Results and Conclusions.

There are two significant scientific results:

1. As wave groups pass, Eulerian counter-flows occur that cancel the Stokes drift variations at the surface.

The magnitude of this counter-flow at the surface exceeds predictions based on an irrotational response (cf. [*Longuet-Higgins and Stewart*, 1962]); namely, that the response approaches half to 2/3 the surface Stokes drift as the wave group length decreases to a single wave. The mechanism by which this counter-flow is generated is not well understood.

2. The Stokes drift due to open ocean surface waves is highly intermittent.

While this is expected even with a Rayleigh distribution of wave amplitudes, appropriate to random seas [*Longuet-Higgins*, 1969b], the observations also show compact wave “packets” (perhaps too short to be called “groups”) that appear to remain coherent for a considerable distance as they propagate. Such coherent packets have not been observed in open ocean deep water conditions previously. As an aside, it may be speculated that since the Eulerian response is of the same order as finite amplitude dispersion corrections, it may be important in understanding wave group dynamics.

In addition, several technical issues have been addressed:

1. The difference between an area-mean velocity based on feature-tracking and one based on area-mean Doppler shifts (“FDV”) has been analyzed and explained in terms of acoustic sheltering of wave crests. The sheltering of crests moves the measurements from being semi-Lagrangian (surface-following) toward being more nearly at a fixed level. For the typical wave steepness, sonar depth, and range interval employed, the analysis suggests that about 1/4 of the Stokes drift remains in the measured means (as opposed to 1/2 for the semi-Lagrangian limit). The effect of a wind-drift layer contributes a small additional deficit to the measurements, making the FDV closer to the full value of Stokes drift (bringing it up to 92%, rather than 75%, as estimated here).

2. Including the FDV (as method 1), three methods were developed to estimate Stokes drift from the data. In particular, methods 2 and 3 permit estimation of the time-space trajectories of Stokes drift anomalies associated with wave groups, in a form directly comparable to that in which the underlying flow is measured. Method 2 makes use of weighted FFT coefficients on the *k*-*f* plane, and is efficient. Method 3 involves detailed extrapolation of the measured velocities to both a fixed level and the moving surface. While more computationally demanding, this also permits explicit estimation of both the Eulerian and fully Lagrangian velocity fields, and also of sheltering and drift current effects.

3. The spatial and temporal extent of the data permit aliased wave variance to be unwrapped in the spectral domain. This effectively extends the resolution of the wave measurements to include the entire portion of the wave spectrum thought most relevant to wave/current interaction dynamics (up to frequencies of order 0.3 Hz).

Acknowledgements. This work was supported by the ONR Physical Oceanography program (C/G N00014-90-J-1285). I thank J. Klymak, R. R. Guza, Pinkel, K. Melville, J. Polton, and many others for useful discussions and suggestions. A big thanks also to the OPG engineering team of E. Slater, M. Goldin, and M. Bui for their tireless efforts to design, construct, deploy, and operate the LRPADS, and in helping to develop the software to analyze the resulting data.

References

Andreas, E.L., J.B. Edson, E.C. Monahan, M.P. Rouault, and S.D. Smith, The Spray Contribution To Net Evaporation From The Sea - A Review Of Recent Progress, *Boundary-Layer Meteorology*, *72* (1-2), 3-52, 1995.

Andrews, D.G., and M.E. McIntyre, An exact theory of nonlinear waves on a Lagrangian mean flow, *J. Fluid Mech.*, *89* (609-646), 1978.

Asher, W.E., L.M. Karle, B.J. Higgins, P.J. Farley, E.C. Monahan, and I.S. Leifer, The Influence Of Bubble Plumes On Air-Seawater Gas Transfer Velocities, *Journal Of Geophysical Research-Oceans*, *101* (5), 12027-12041, 1996.

Banner, M.L., and O.M. Phillips, On the incipient breaking of small scale waves, *Journal of Fluid Mechanics*, *65*, 647-656, 1974.

Brumley, B.H., R.G. Cabrera, K.L. Deines, and E.A. Terray, Performance of a broad-band acoustic Doppler current profiler, *IEEE J. Oceanic Eng.*, *16* (4), 402-407, 1991.

Craik, A.D.D., The generation of Langmuir circulation by an instability mechanism, *J. Fluid Mech.*, *81*, 209-223, 1977.

Craik, A.D.D., and S. Leibovich, A rational model for Langmuir circulations, *J. Fluid Mech.*, *73*, 401-426, 1976.

Crawford, C.B., and D.M. Farmer, On the spatial distribution of ocean bubbles, *J. Geophys. Res.*, *92* (C8), 8231-8243, 1987.

Edson, J.B., and C.W. Fairall, Spray Droplet Modeling .1. Lagrangian Model Simulation of the Turbulent Transport of Evaporating Droplets, *Journal of Geophysical Research-Oceans*, *99* (C12), 25295-25311, 1994.

Garrett, C., Generation of Langmuir circulations by surface waves– A feedback mechanism, *J. Mar. Res.*, *34*, 117-130, 1976.

Grimshaw, R., Mean flows generated by a progressing water wave packet, *J. Austral. Math. Soc. B*, *22*, 318-347, 1981.

Groeneweg, J., and G. Klopman, Changes of the Mean Velocity Profiles in the Combined Wave-Current Motion Described in a GLM Formulation, *Journal of Fluid Mechanics*, *370*, 271-296, 1998.

Hara, T., and S.E. Belcher, Wind forcing in the equilibrium range of wind-wave spectra, *Journal of Fluid Mechanics*, *470*, 223-245, 2002.

Herbers, T.H.C., S. Elgar, and R.T. Guza, Infragravity-frequency (0.005-0.05 Hz) motions on the shelf, Part 1: Forced waves, *Journal Of Physical Oceanography*, *24* (5), 917-927, 1994.

Jiang, J.-Y., and R.L. Street, Modulated flows beneath wind-ruffled, mechanically generated water waves, *J. Geophys. Res. (Oceans)*, *98* (C2), 2711-2721, 1991.

Kemp, P.H., and R.R. Simons, The interaction of waves and a turbulent current; waves propagating with the current, *J. Fluid Mech.*, *116*, 227-250, 1982.

Kemp, P.H., and R.R. Simons, The interaction of waves and a turbulent current; waves propagating against the current, *J. Fluid Mech.*, *130*, 73-89, 1983.

Langmuir, I., Surface motion of water induced by wind, *Science*, *87* (2250), 119-123, 1938.

Leibovich, S., Convective instability of stably stratified water in the ocean, *J. Fluid Mech.*, *82*, 561-581, 1977.

Leibovich, S., On wave-current interaction theories of Langmuir circulations, *J. Fluid Mech.*, *99*, 715-724, 1980.

Li, M., K. Zahariev, and C. Garrett, Role of Langmuir circulation in the deepening of the ocean surface mixed layer, *Science*, *270*, 1955-1957, 1995.

Longuet-Higgins, M.S., Mass transport in water waves, *Phil. Trans.*, *A 245*, 535-581, 1953.

Longuet-Higgins, M.S., Action of a variable stress at the surface of water waves, *Phys. of Fluids*, *12*, 737, 1969a.

Longuet-Higgins, M.S., On wave breaking and the equilibrium spectrum of wind generated waves, *Proc. Roy. Soc.*, *A311*, 371-389, 1969b.

Longuet-Higgins, M.S., and R.W. Stewart, Changes in the form of short gravity waves on long waves and tidal currents, *J. Fluid Mech.*, *8*, 565-583, 1960.

Longuet-Higgins, M.S., and R.W. Stewart, Short gravity waves on steady non-uniform currents, *J. Fluid Mech.*, *10*, 529, 1961.

Longuet-Higgins, M.S., and R.W. Stewart, Radiation stress and mass transport in gravity waves, with application to 'surf-beats', *J. Fluid Mech.*, *13*, 481-504, 1962.

Longuet-Higgins, M.S., and R.W. Stewart, Radiation stress in water waves; a physical discussion, with applications, *Deep Sea Res.*, *11*, 529-562, 1964.

McWilliams, J.C., and P.P. Sullivan, Vertical mixing by Langmuir circulations, *Spill Science & Technology Bulletin*, *6* (3-4), 225-237, 2000.

McWilliams, J.C., P.P. Sullivan, and C.H. Moeng, Langmuir turbulence in the ocean, *J. Fluid Mech.*, *334* (334), 1-30, 1997.

Monismith, S.G., E.A. Cowen, H.M. Nepf, J. Magnaudet, and L. Thais, Mean flows under surface gravity waves, *(unpublished manuscript)*, 1996.

Pattison, M.J., and S.E. Belcher, Production rates of sea-spray droplets, *Journal of Geophysical Research-Oceans*, *104* (C8), 18397-18407, 1999.

Phillips, W.R.C., Langmuir circulations beneath growing or decaying surface waves, *Journal of Fluid Mechanics*, *469*, 317-342, 2002.

Pinkel, R., and J.A. Smith, Repeat-sequence coding for improved precision of Doppler sonar and sodar, *J. Atmos. Oceanic Technol.*, *9* (2), 149-163, 1992.

Plant, W.J., and J. Wright, Phase speeds of upwind and downwind travelling short gravity waves, *J. Geophys. Res.*, *85*, 3304-3310, 1980.

Rudnick, D.L., T.J. Boyd, R.E. Brainard, G.S. Carter, G.D. Egbert, M.C. Gregg, P.E. Holloway, J.M. Klymak, E. Kunze, C.M. Lee, M.D. Levine, D.S. Luther, J.P. Martin, M.A. Merrifield, J.N. Moum, J.D. Nash, R. Pinkel, L. Rainville, and T.B. Sanford, From tides to mixing along the Hawaiian ridge, *Science*, *301* (5631), 355-357, 2003.

Rummler, W.D., Introduction of a new estimator for velocity spectral parameters., AT&T Bell Labs., Murray Hill, N.J., 1968.

Skyllingstad, E.D., and D.W. Denbo, An ocean large-eddy simulation of Langmuir circulations and convection in the surface mixed layer, *J. Geophys. Res.*, *100* (5), 8501-8522, 1995.

Smith, J.A., Short surface waves with growth and dissipation, *J. Geophys. Res.*, *91* (C2), 2616-2632, 1986.

Smith, J.A., Modulation of short wind waves by long waves, in *Surface Waves and Fluxes: Current Theory and Remote Sensing*, edited by G.L. Geernaert, and W.J. Plant, pp. 247- 284, Kluwer Academic Publishers, the Netherlands, 1990.

Smith, J.A., Observed growth of Langmuir circulation, *J. Geophys. Res.*, *97*, 5651-5664, 1992.

Smith, J.A., Evolution of Langmuir circulation during a storm, *Journal of Geophysical Research*, *103* (C6), 12,649-12,668, 1998.

Smith, J.A., Continuous time-space sampling of near-surface velocities using sound, *J. Atmos. Oceanic Tech.*, *19* (11), 1860-1872, 2002.

Smith, J.A., and G.T. Bullard, Directional Surface Wave Estimates from Doppler Sonar Data, *Journal of Atmospheric and Oceanic Technology*, *12* (3), 617-632, 1995.

Stokes, G.G., On the theory of oscillatory waves, *Trans. Camb. Phil. Soc.*, *8*, 441-455, 1847.

Sullivan, P.P., J.C. McWilliams, and W.K. Melville, The oceanic boundary layer driven by wave breaking with stochastic variability. Part 1. Direct numerical simulations, *Journal of Fluid Mechanics*, *507*, 143-174, 2004.

Swan, C., Convection within an experimental wave flume, *J. Hydraul. Res.*, *28*, 273-282, 1990.

Terray, E.A., M.A. Donelan, Y.C. Agrawal, W.M. Drennan, K.K. Kahma, A.J. Williams, P.A. Hwang, and S.A. Kitaigorodskii, Estimates Of Kinetic Energy Dissipation Under Breaking Waves, *Journal Of Physical Oceanography*, *26* (5), 792-807, 1996.

Theriault, K.B., Incoherent Multibeam Doppler current profiler performance. Part I: estimate variance., *Journal of Ocean Engineering*, *OE-11* (1), 7-15, 1986.

Thompson, R.O.R.Y., Coherence significance levels, *J. Atmos. Sci.*, *36*, 2020-2021, 1979.

Thorpe, S.A., On the clouds of bubbles formed by breaking wind waves in deep water, and their role in air-sea gas transfer., *Philos. Trans. R. Soc. London, Ser. A*, *304*, 155-210, 1982.

Thorpe, S.A., Bubble clouds: A review of their detection by sonar, of related models, and of how K_v may be determined., in *Oceanic Whitecaps and Their Role in Air-Sea Exchange Processes*, edited by E.C.M.a.G.M. Noicall, pp. 57-68, D. Reidel, Norwell, Mass., 1986.

Trevorrow, M.V., and D.M. Farmer, The use of Barker codes in Doppler sonar measurements, *J. Atmos. Oceanic Technol.*, *9* (5), 699-704, 1992.

Wu, J., Wind-induced drift currents, *J. Fluid Mech.*, *68*, 49-70, 1975.

Zappa, C.J., W.E. Asher, A.T. Jessup, J. Klinke, and S.R. Long, Microbreaking and the enhancement of air-water transfer velocity - art. no. C08S16, *Journal of Geophysical Research-Oceans*, *109* (C8), S816, 2004.

Zilitinkevich, S.S., A.A. Grachev, and C.W. Fairall, Scaling reasoning and field data on the sea surface roughness lengths for scalars, *Journal of the Atmospheric Sciences*, *58* (3), 320-325, 2001.

Figure Captions

Figure 1. Location of Research Platform FLIP (Floating Instrument Platform) during the near-field leg of HOME (Hawaii Ocean Mixing Experiment), September through October 2002. The site is about 20 miles ENE of Oahu, over an underwater ridge that extends roughly halfway to Kauai. Depth contour interval is 1000 m, deepest shown is 4000 m. (the abyssal plain is 5000 m, so that contour is messy and hence is omitted). Data contoured are 2 minute resolution, from NGDC.

Figure 2. (Upper) Wind speed at FLIP and (lower) tidal elevation at Honolulu during the time of the LRPADS deployment off Oahu. Whenever the wind is over 5 m/s, it comes from between 90 and 100° (re. true North).

Figure 3. Two views of the surface wave field. (Left) The radial slope; (right) radial surface orbital velocity component. The black arrow indicates the wind direction and magnitude (near 10 m/s). The dominant waves have roughly 10 s period, and are propagating downwind.

Figure 4. Feature-tracking velocity minus 1.25% W_{10} (black) versus mean Doppler velocity (red) over the time the LRPADS was deployed. There is close correspondence. The Eastward Doppler is roughly along the axis of the LRPADS sample area; the Northward component is estimated from the trend with angle, so it is slightly more noisy. The feature-tracking algorithm is less sensitive to direction, but is a bit more noisy overall, especially during calm periods when there are fewer embedded features to track.

Figure 5. Feature-tracking minus Doppler-based velocity estimates ($V_{feature} - V_{Doppler}$ or "FDV"; black lines) versus 1.25% W_{10} (red) over the time the LRPADS was deployed. The latter is a good "rule of thumb" estimate of the surface Stokes drift. The former is thought to be tightly related to the actual Stokes drift (see text), although somewhat noisy. The overall correspondence between the two estimates is good. Note the anti-phase oscillations at tidal frequencies in the two estimates of the

Eastward component on days 272 through 276. A negative Eastward component corresponds to downwind flow, since the wind is from the East.

Figure 6. Schematic plot of acoustic sheltering of wave crests. (Black) the simulated surface elevation; (red) the "sheltered depths" or upper limit of acoustic probing. Red rays also show some of the acoustic paths from the sonar (at 15 m depth). For typical wave conditions, sheltering does not occur before about 150 m range.

Figure 7. Time-mean velocity differences in the simulated data. (black line) Synthetic measured velocity minus the Eulerian reference, $U_m - U_0$; (green line) Surface velocity minus Eulerian, $U_\zeta - U_0$; (blue line) the theoretical $< U_\zeta - U_0 >$ for the input spectral lines. The synthetic measured velocity is at the calculated sheltered depth; the Eulerian velocity is at fixed depth z = –RMS(ζ); the semi-Lagrangian velocity is at the surface ($z = \zeta$), but not displaced horizontally. The green and blue lines should both correspond to half the Stokes drift.

Figure 8. The sheltering thickness (depth of upper acoustic sampling limit below the actual surface; values are positive only), estimated from field data. Elevation is estimated (see section 5, eq. 5.17), then the acoustic shading algorithm is applied. Since waves propagating at right angles to the beam are ineffective at sheltering, the loss of sensitivity in the data to such waves is unimportant in this calculation. The estimated deficit in wind-drift due to sheltering looks very similar (but with a scale-change from 1 m to about 15 cm/s)

Figure 9. The time-mean reduction in measured surface drift due to sheltering, for a wind-drift with depth scale 1 m and surface magnitude 16 cm/s. This effect contributes to the difference between the feature-track and Doppler derived means (FDV), increasing it from 75% to roughly 92% of the estimated value of Stokes drift.

Figure 10. Time-range plot of radial velocities, dominated by the surface waves' orbital velocity. The spectral peak is near 0.1 Hz; note a large wave group starting near 0 m range at 300 s, and moving out to1000 m range by 435 s, corresponding to a group velocity of about 7.5 m/s. Several thinner "slashes" are seen propagating a little slower, at a speed of about 5 m/s. These slashes are compact wave groups of order one wavelength long (along the vertical axis; i.e. spatially). The frequency associated with these compact groups is near 0.14 Hz (7 s period). The group speed is about 5 m/s, and the corresponding phase speed is about equal to the wind speed, 10 m/s.

Figure 11. Wavenumber-frequency (*k*–*f*) spectra for a typical 8.5 minute segment from the HOME data set (Oct 4, 2002, 14:56:48 HDT): (left panel) backscatter intensity, and (right panel) radial velocity. Nominally negative frequencies are appended to the right of the positive ones. The surface wave variance continues across the Nyquist frequency (f_{NY} = 0.2 Hz) to alias onto the right halves (see red outlines, delimiting wave variance). It continues to alias across the Nyquist wavenumber (k_{NY} = 0.047) as well (yellow horizontal line), wrapping back onto the portion of the spectrum corresponding to slower moving phenomena (the green outlines correspond to the wavenumber-aliases of the red ones). The waves are predominantly directed downwind, allowing the ambiguities of aliased variance to be resolved. The unwrapped and masked *k*–*f* spectrum can be inverse-transformed, effectively interpolating the wave data to twice the time sampling and 1.5 times the spatial sampling rates. Note that in the velocity spectrum (right panel) the next most prominent feature after the waves is a ridge of variance along a line corresponding to 5 m/s, while in the intensity data (left panel) it is variance embedded in the mean flow (near the vertical axis), and the signal along the 5 m/s ridge is not significant.

Figure 12. Wavenumber-frequency spectrum for re-sampled data (7.5 m range resolution; k_{NY} = 0.065 cycles/m) from the same time as figures 10, 11. (Left) Full spectrum with aliased data; (right) spectrum with aliased data masked off. Note that in addition to the surface wave variance (outlined in red on the left), a weaker ridge of variance lies along a line at roughly 45°, corresponding to propagation at about 5 m/s. This variance is broadly distributed in *k* and *f*, however, so it would be difficult to isolate

without both the k and f information. The red lines are also used to delimit the separation between "wave-like" from "non-wave" variance in the spectral domain.

Figure 13. Mean estimated radial component of Stokes drift U_S for the same time and beam as shown in figure 10. (Black) U_S from twice the difference between U_ζ and U_0 (eq. 5.16); (red) U_S from the magnitude-squared of adjusted spectral coefficients (eq. 5.13). (Green, blue) Same, respectively, but adjusted by a linear increase with range (see section 6).

Figure 14. Time-range plot of the radial Stokes drift for the same segment as in the previous figures (time-means at each range are removed; see figure 13). Note the predominance of red "slashes" at an angle corresponding to roughly 5 m/s propagation along the beam. Comparing this with figure 10, it can be seen that these are associated with the smaller-scale but intense "packets" of 7 s waves, rather than with the larger-scale 10 s waves.

Figure 15. Spatial distribution of radial velocity associated with the ridge of variance along the 5 m/s line in the k–f spectra. A spectral filter passing variance moving between 4.5 and 6.5 m/s (in either direction along each beam) was applied. The background "speckle" of ± 3 cm/s or so is the noise level of the measurement as filtered. The darker blue band seen near 700 m range on the left and near 800 m on the right is the motion associated with the 5 m/s line. The two frames shown are 20 s apart. The black arrow indicates the wind direction and speed (~10 m/s); the red arrow indicates the mean current (~15 cm/s). The feature is short in the alongwind direction, long in the crosswind direction, and moving at about 5 m/s.

Figure 16. Time-range plot of the wave-filtered radial Eulerian velocity U_0 along one beam. There is a predominance of blue slashes rising to the right, propagating at about 5 m/s. There is some resemblance to the red slashes seen in the plot of Stokes drift (figure 15).

Figure 17. Time-range plot of the wave-filtered radial Lagrangian velocity $U_L = U_0 + U_S$ for the same data as figure 18. The cancellation of variance is quite complete at all resolved scales, leaving essentially an image of the filtered measurement noise.

Figure 18. Wavenumber-frequency spectra for (left) the Eulerian velocity field and (right) the Lagrangian velocity field formed by adding the Eulerian and Stokes drift estimates. The reduction in variance along the 5 m/s line in the Lagrangian field is dramatic. Because the means are not well determined, some variance is to be expected near the origin. Comparison of the spectral levels at + and – k values for the same frequencies indicates that there is no longer any preferential direction; the remainder probably represents the spectral noise floor. In particular, note that there is no significant signal in the Lagrangian spectral densities for wavenumbers over roughly 0.005 cycles/m.

Figure 19. Coherence between U_S and $-U_0$ versus range, as estimated from time averages: $-\langle U_S U_0 \rangle / [\langle U_S^2 \rangle \langle U_0^2 \rangle]^{1/2}$ (both for wave-filtered velocities; note minus sign). As indicated by the level of jitter, the standard deviation of the coherence estimate is less than 0.1. The 95% level is about 0.12, and the coherence levels are several times larger than this.

Figure 20. The transfer coefficient from Stokes drift U_S to the negative Eulerian velocity anomaly (wave-filtered) $-U_0$: $T_C = -\langle U_S U_0 \rangle / \langle U_S^2 \rangle$. This starts very near 1.0 at near ranges, indicating that the correlated part of the two fields cancel out. A value over 1 indicates an Eulerian anomaly larger than the Stokes drift, contrary to expectations. As range increases, the Stokes drift is probably underestimated slightly due to finite spatial smoothing. The increase in transfer coefficient with range is likely attributable to this, and might serve as a guide in compensating for this underestimation (see figure 13). There is every indication that the response is no smaller than the Stokes drift, and is most likely a one-to-one match.

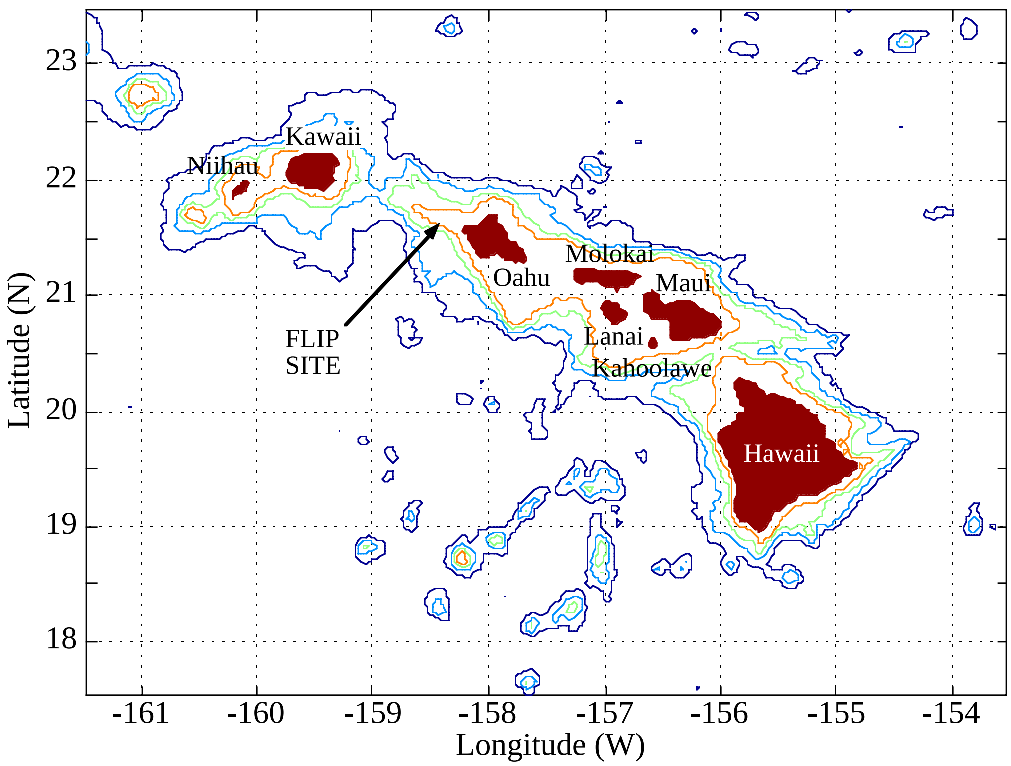

Figure 1. Location of Research Platform FLIP (Floating Instrument Platform) during the near-field leg of HOME (Hawaii Ocean Mixing Experiment), September through October 2002. The site is about 20 miles ENE of Oahu, over an underwater ridge that extends roughly halfway to Kauai. Depth contour interval is 1000 m, deepest shown is 4000 m. (the abyssal plain is 5000 m, so that contour is messy and hence is omitted). Data contoured are 2 minute resolution, from NGDC.

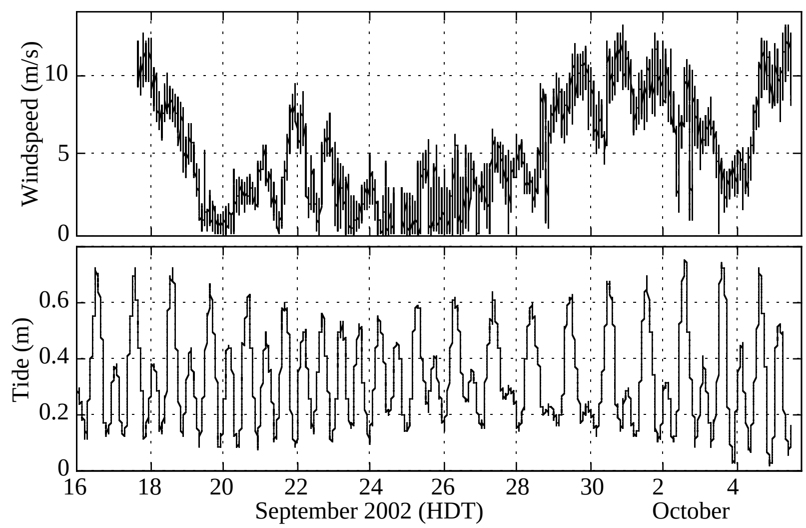

Figure 2. (Upper) Wind speed at FLIP and (lower) tidal elevation at Honolulu during the time of the LRPADS deployment off Oahu. Whenever the wind is over 5 m/s, it comes from between 90 and 100° (re. true North).

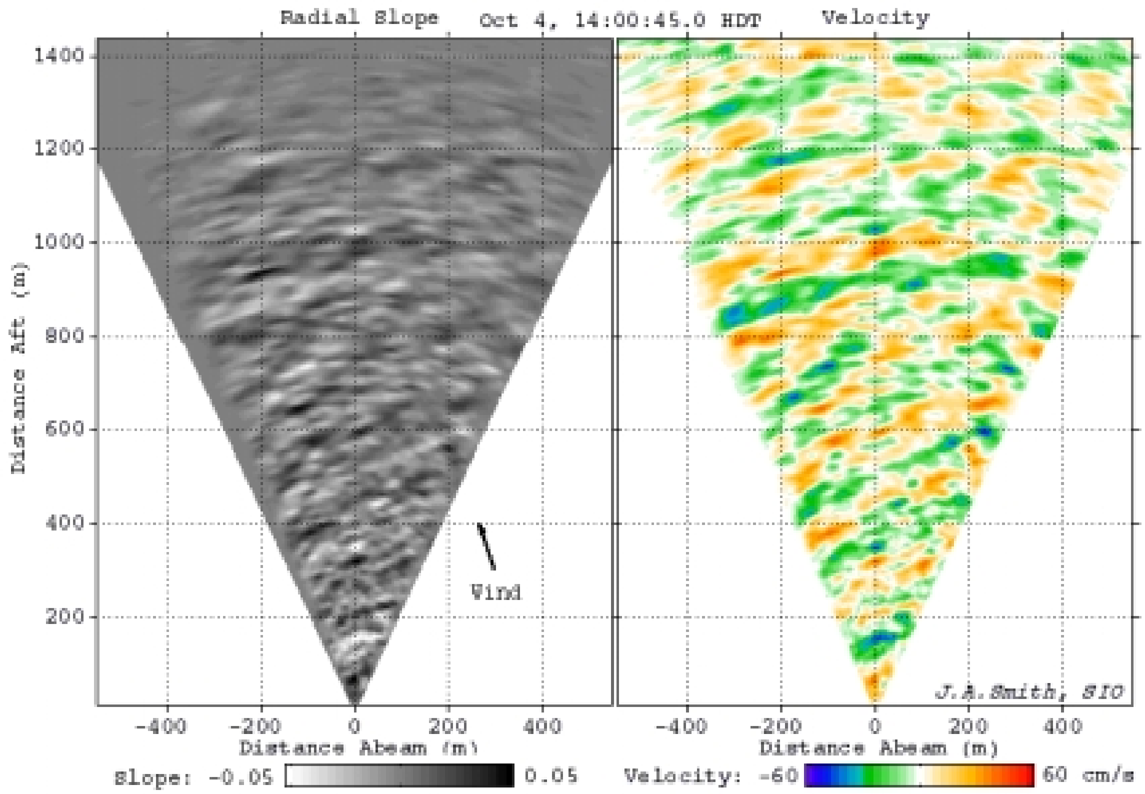

Figure 3. Two views of the surface wave field. (Left) The radial slope; (right) radial surface orbital velocity component. The black arrow indicates the wind direction and magnitude (near 10 m/s). The dominant waves have roughly 10 s period, and are propagating downwind.

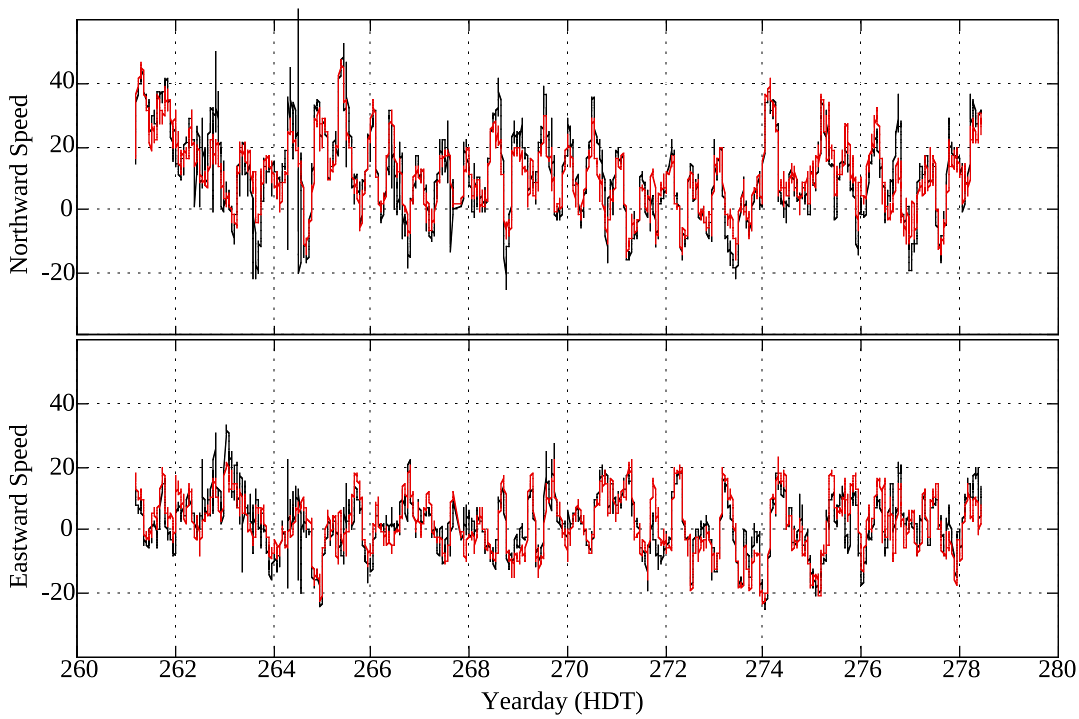

Figure 4. Feature-tracking velocity minus 1.25% W_{10} (black) versus mean Doppler velocity (red) over the time the LRPADS was deployed. There is close correspondence. The Eastward Doppler is roughly along the axis of the LRPADS sample area; the Northward component is estimated from the trend with angle, so it is slightly more noisy. The feature-tracking algorithm is less sensitive to direction, but is a bit more noisy overall, especially during calm periods when there are fewer embedded features to track.

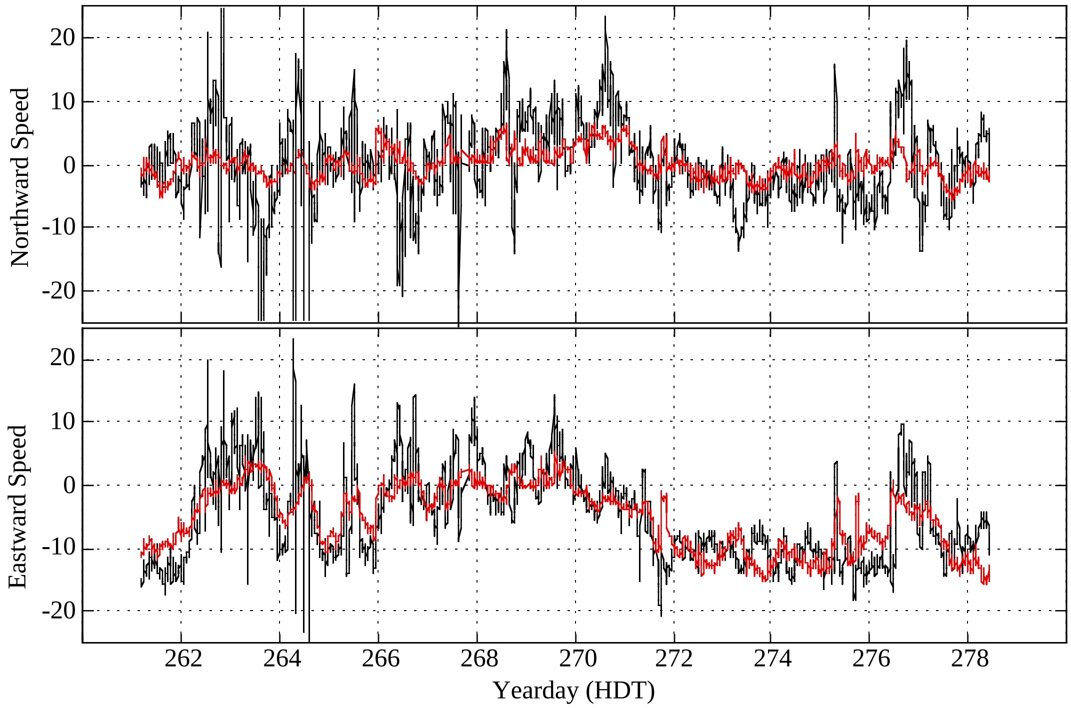

Figure 5. Feature-tracking minus Doppler-based velocity estimates ($V_{feature} - V_{Doppler}$ or "FDV"; black lines) versus 1.25% W_{10} (red) over the time the LRPADS was deployed. The latter is a good "rule of thumb" estimate of the surface Stokes drift. The former is thought to be tightly related to the actual Stokes drift (see text), although somewhat noisy. The overall correspondence between the two estimates is good. Note the anti-phase oscillations at tidal frequencies in the two estimates of the Eastward component on days 272 through 276. A negative Eastward component corresponds to downwind flow, since the wind is from the East.

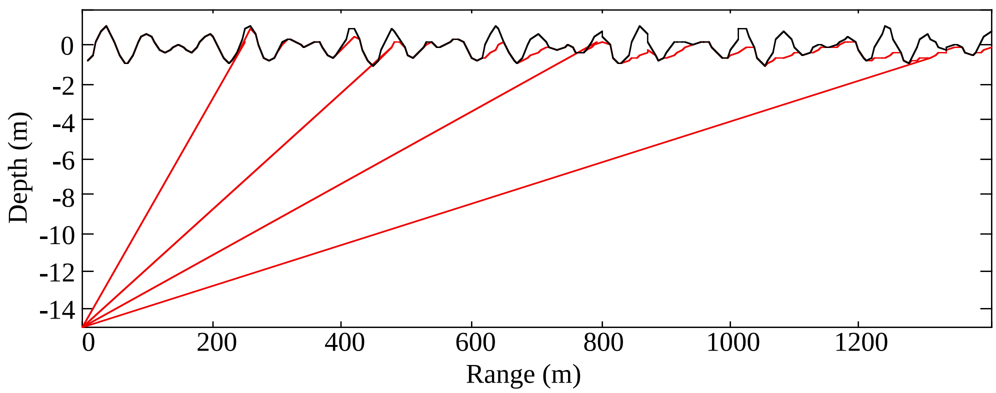

Figure 6. Schematic plot of acoustic sheltering of wave crests. (Black) the simulated surface elevation; (red) the "sheltered depths" or upper limit of acoustic probing. Red rays also show some of the acoustic paths from the sonar (at 15 m depth). For typical wave conditions, sheltering does not occur before about 150 m range.

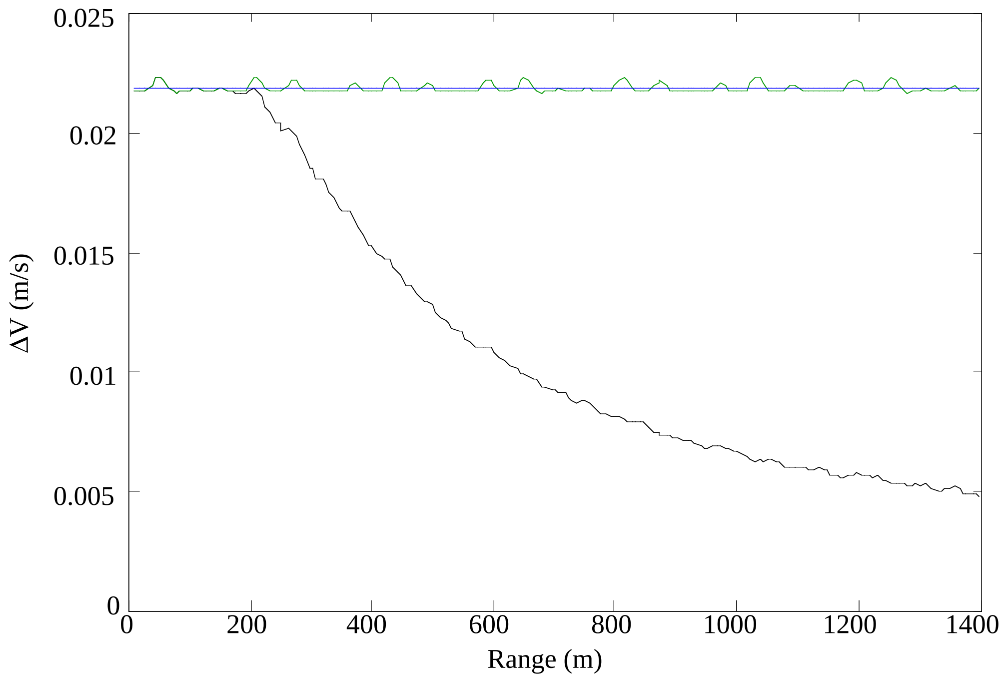

Figure 7. Time-mean velocity differences in the simulated data. (black line) Synthetic measured velocity minus the Eulerian reference, $U_m - U_0$; (green line) Surface velocity minus Eulerian, $U_\zeta - U_0$; (blue line) the theoretical $\langle U_\zeta - U_0 \rangle$ for the input spectral lines. The synthetic measured velocity is at the calculated sheltered depth; the Eulerian velocity is at fixed depth $z = -\mathrm{RMS}(\zeta)$; the semi-Lagrangian velocity is at the surface ($z = \zeta$), but not displaced horizontally. The green and blue lines should both correspond to half the Stokes drift.

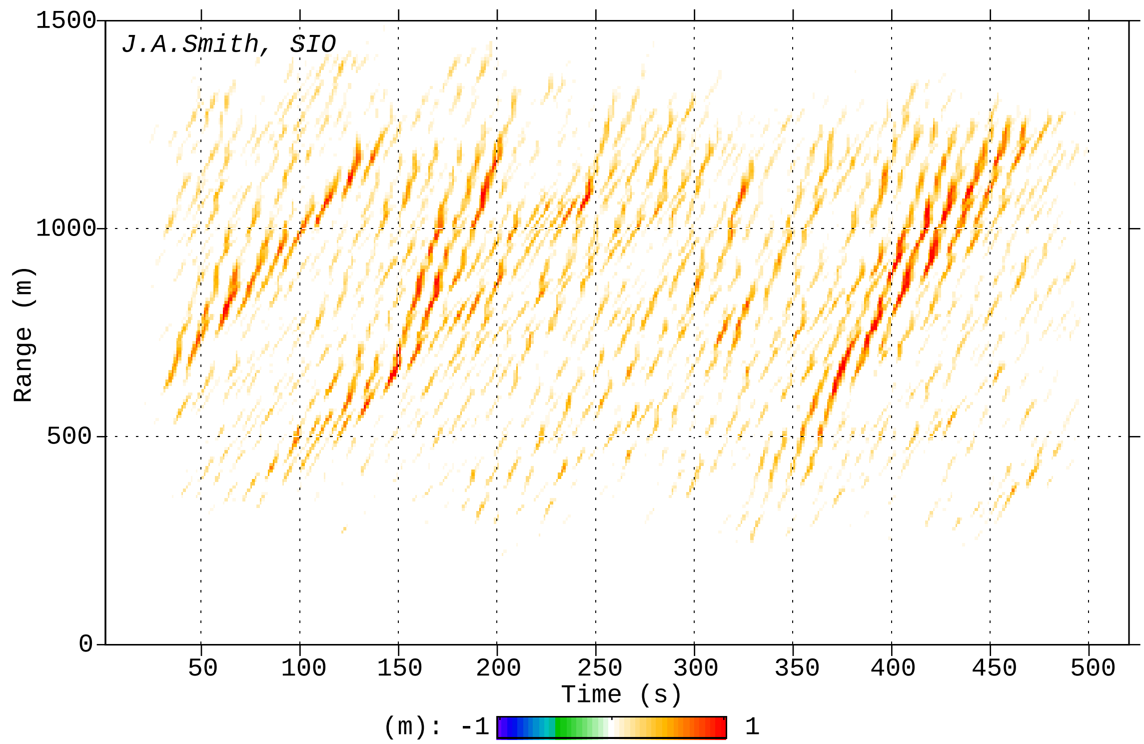

Figure 8. The sheltering thickness (depth of upper acoustic sampling limit below the actual surface; values are positive only), estimated from field data. Elevation is estimated (see section 5, eq. 5.17), then the acoustic shading algorithm is applied. Since waves propagating at right angles to the beam are ineffective at sheltering, the loss of sensitivity in the data to such waves is unimportant in this calculation. The estimated deficit in wind-drift due to sheltering looks very similar (but with a scale-change from 1 m to about 15 cm/s)

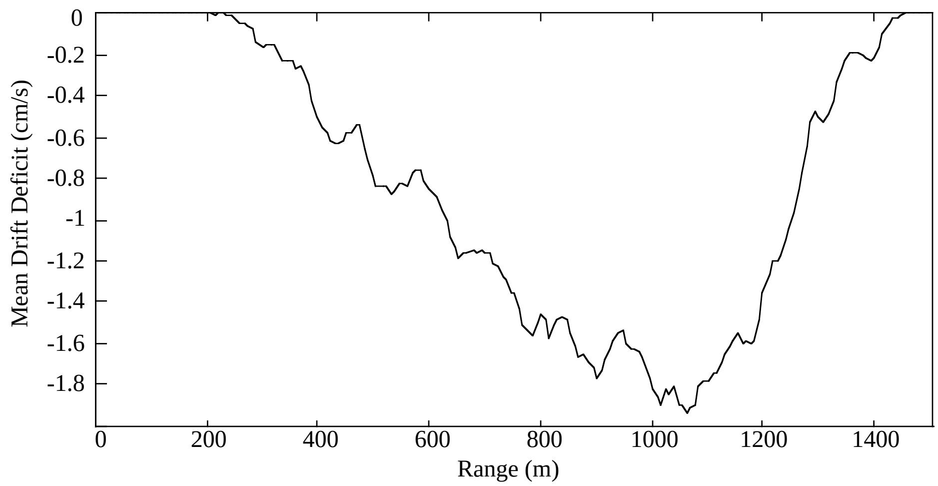

Figure 9. The time-mean reduction in measured surface drift due to sheltering, for a wind-drift with depth scale 1 m and surface magnitude 16 cm/s. This effect contributes to the difference between the feature-track and Doppler derived means (FDV), increasing it from 75% to roughly 92% of the estimated value of Stokes drift.

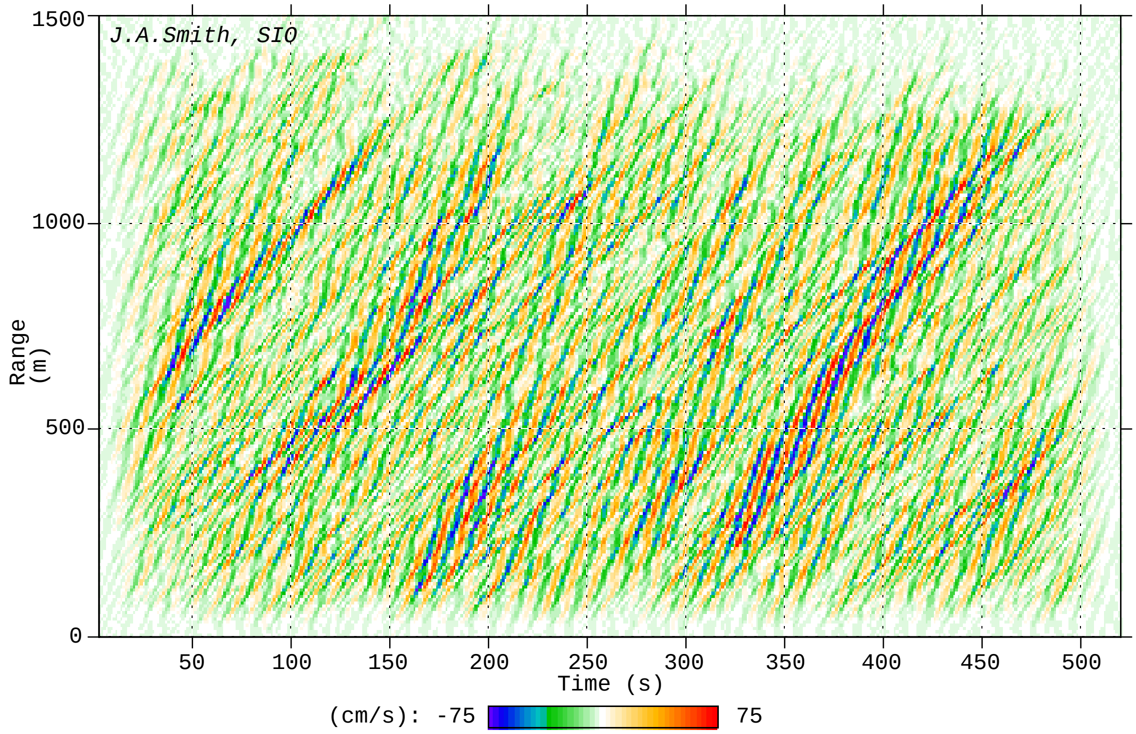

Figure 10. Time-range plot of radial velocities, dominated by the surface waves' orbital velocity. The spectral peak is near 0.1 Hz; note a large wave group starting near 0 m range at 300 s, and moving out to1000 m range by 435 s, corresponding to a group velocity of about 7.5 m/s. Several thinner "slashes" are seen propagating a little slower, at a speed of about 5 m/s. These slashes are compact wave groups of order one wavelength long (along the vertical axis; i.e. spatially). The frequency associated with these compact groups is near 0.14 Hz (7 s period). The group speed is about 5 m/s, and the corresponding phase speed is about equal to the wind speed, 10 m/s.

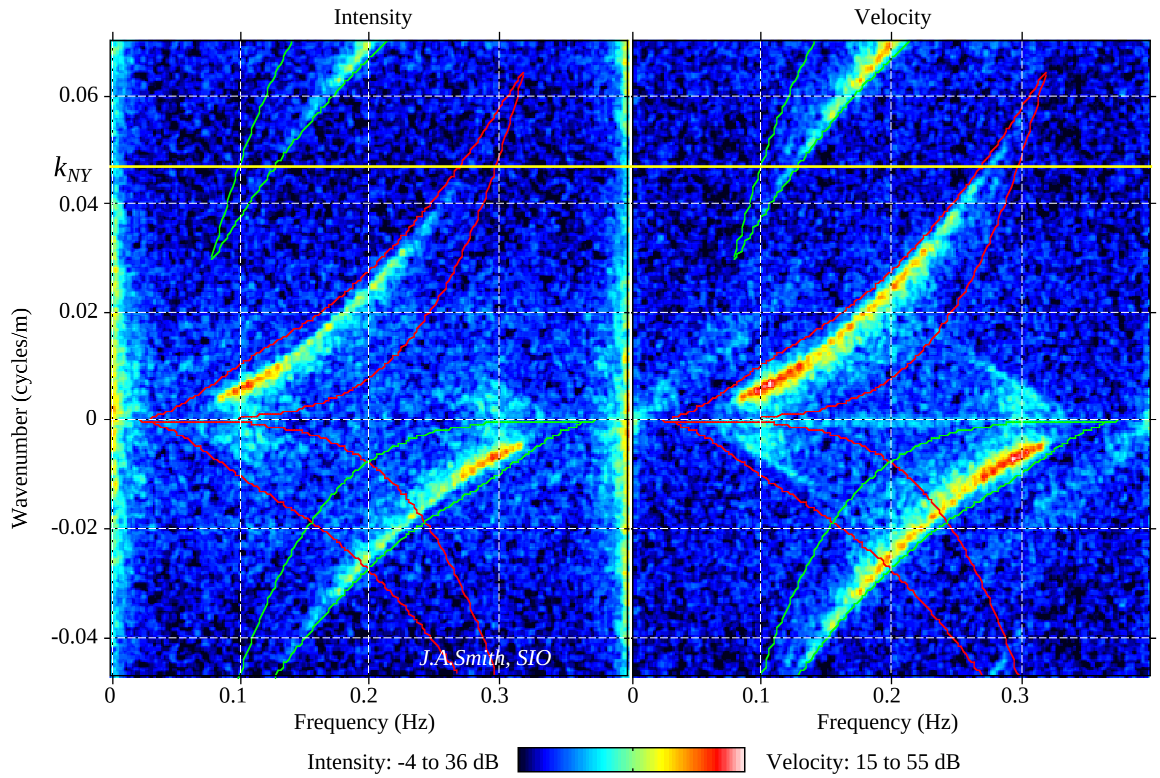

Figure 11. Wavenumber-frequency (k–f) spectra for a typical 8.5 minute segment from the HOME data set (Oct 4, 2002, 14:56:48 HDT): (left panel) backscatter intensity, and (right panel) radial velocity. Nominally negative frequencies are appended to the right of the positive ones. The surface wave variance continues across the Nyquist frequency (f_{NY} = 0.2 Hz) to alias onto the right halves (see red outlines, delimiting wave variance). It continues to alias across the Nyquist wavenumber (k_{NY} = 0.047) as well (yellow horizontal line), wrapping back onto the portion of the spectrum corresponding to slower moving phenomena (the green outlines correspond to the wavenumber-aliases of the red ones). The waves are predominantly directed downwind, allowing the ambiguities of aliased variance to be resolved. The unwrapped and masked k–f spectrum can be inverse-transformed, effectively interpolating the wave data to twice the time sampling and 1.5 times the spatial sampling rates. Note that in the velocity spectrum (right panel) the next most prominent feature after the waves is a ridge of variance along a line corresponding to 5 m/s, while in the intensity data (left panel) it is variance embedded in the mean flow (near the vertical axis), and the signal along the 5 m/s ridge is not significant.

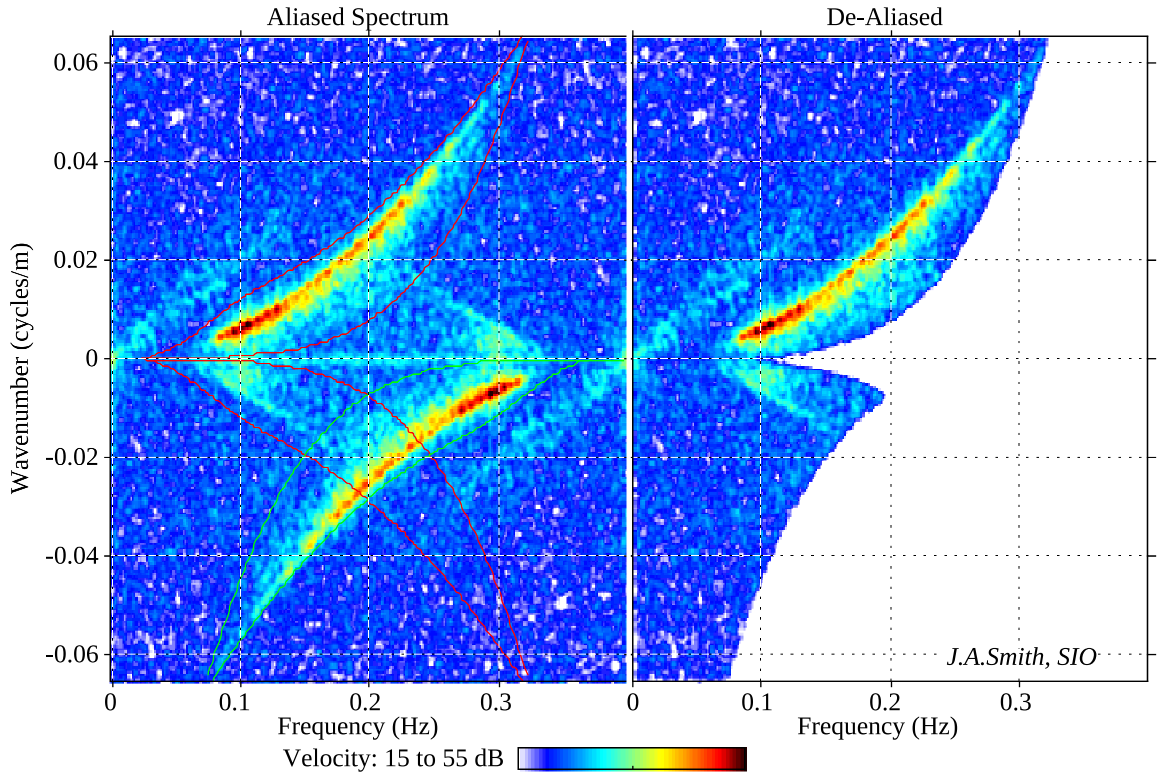

Figure 12. Wavenumber-frequency spectrum for re-sampled data (7.5 m range resolution; k_{NY} = 0.065 cycles/m) from the same time as figures 10, 11. (Left) Full spectrum with aliased data; (right) spectrum with aliased data masked off. Note that in addition to the surface wave variance (outlined in red on the left), a weaker ridge of variance lies along a line at roughly 45°, corresponding to propagation at about 5 m/s. This variance is broadly distributed in *k* and *f*, however, so it would be difficult to isolate without both the *k* and *f* information. The red lines are also used to delimit the separation between "wave-like" from "non-wave" variance in the spectral domain.

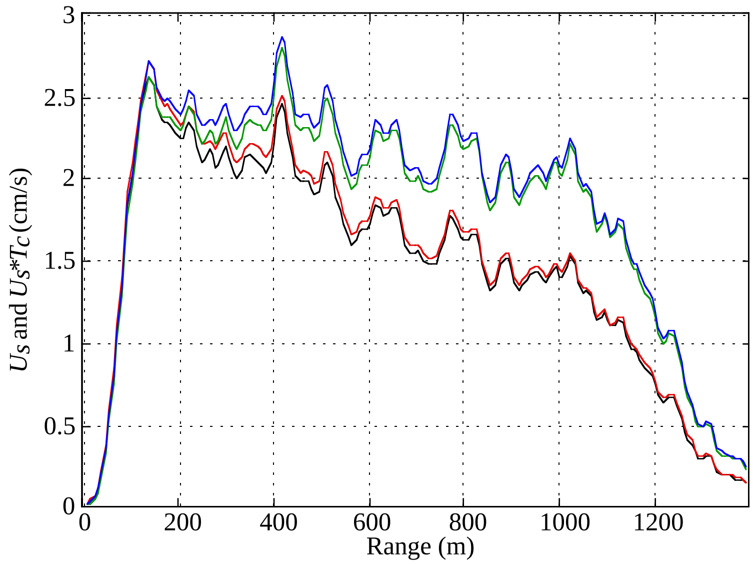

Figure 13. Mean estimated radial component of Stokes drift U_S for the same time and beam as shown in figure 10. (Black) U_S from twice the difference between U_ζ and U_0 (eq. 5.16); (red) U_S from the magnitude-squared of adjusted spectral coefficients (eq. 5.13). (Green, blue) Same, respectively, but adjusted by a linear increase with range (see section 6).

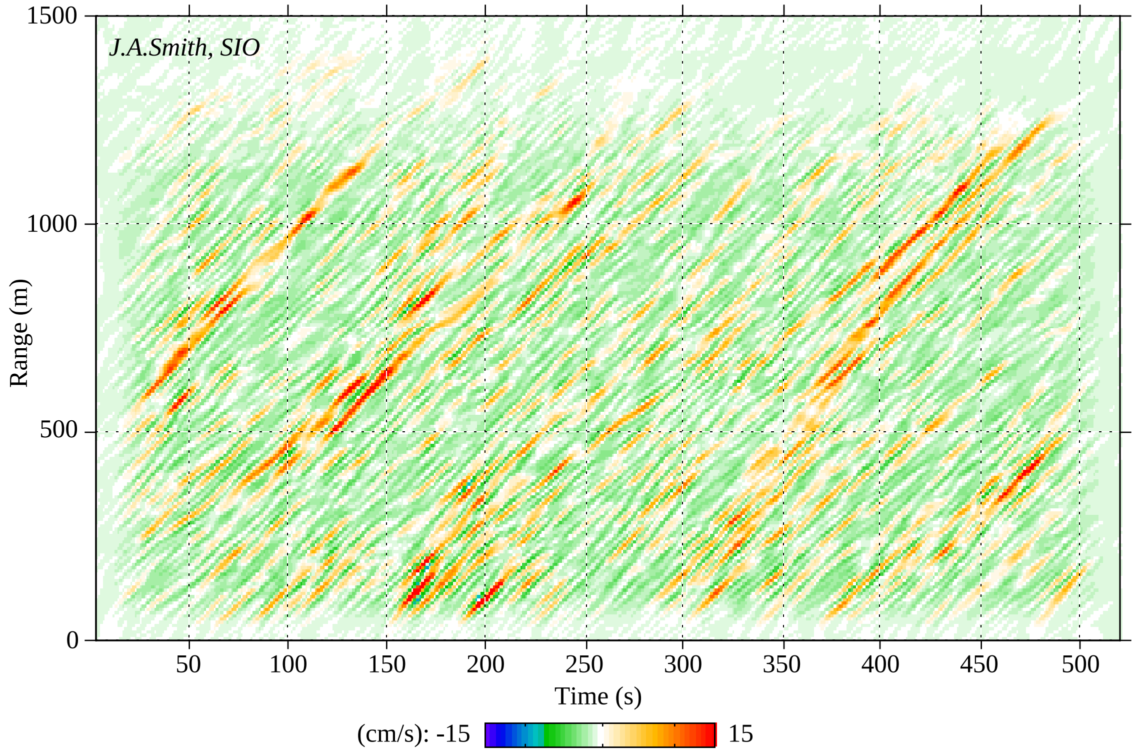

Figure 14. Time-range plot of the radial Stokes drift for the same segment as in the previous figures (time-means at each range are removed; see figure 13). Note the predominance of red "slashes" at an angle corresponding to roughly 5 m/s propagation along the beam. Comparing this with figure 10, it can be seen that these are associated with the smaller-scale but intense "packets" of 7 s waves, rather than with the larger-scale 10 s waves.

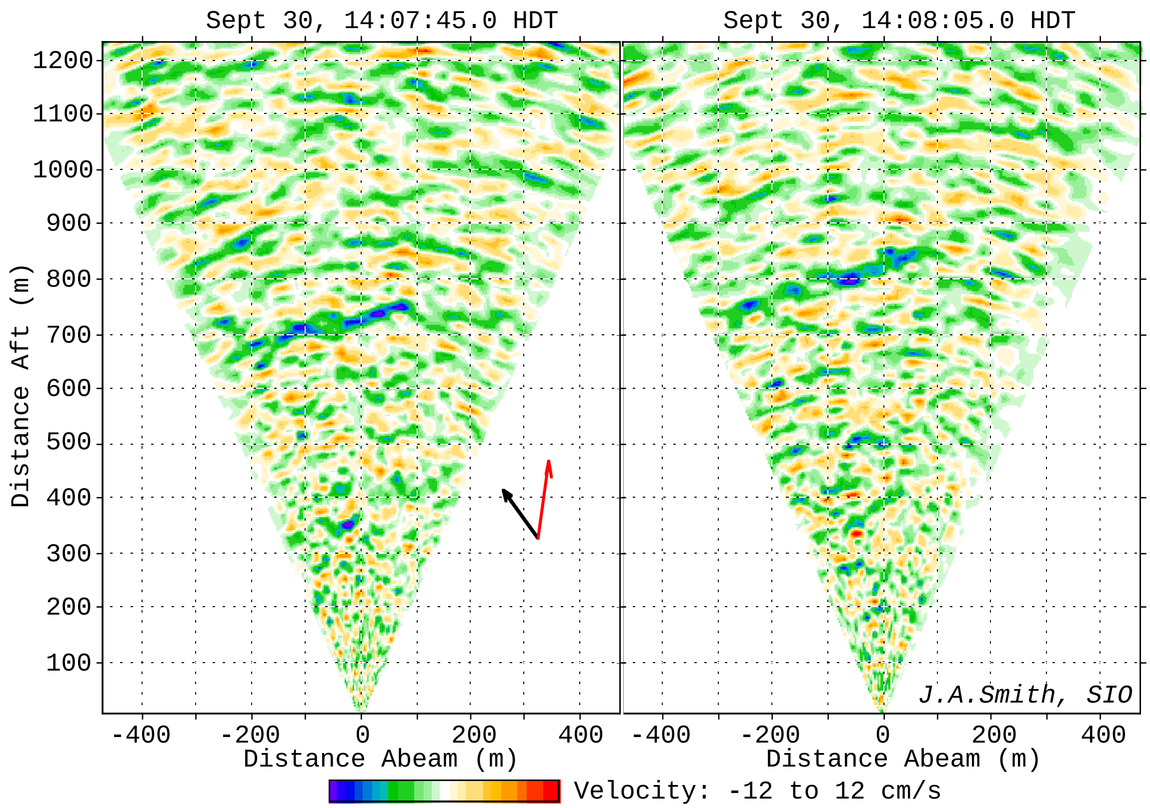

Figure 15. Spatial distribution of radial velocity associated with the ridge of variance along the 5 m/s line in the *k–f* spectra. A spectral filter passing variance moving between 4.5 and 6.5 m/s (in either direction along each beam) was applied. The background "speckle" of ± 3 cm/s or so is the noise level of the measurement as filtered. The darker blue band seen near 700 m range on the left and near 800 m on the right is the motion associated with the 5 m/s line. The two frames shown are 20 s apart. The black arrow indicates the wind direction and speed (~10 m/s); the red arrow indicates the mean current (~15 cm/s). The feature is short in the alongwind direction, long in the crosswind direction, and moving at about 5 m/s.

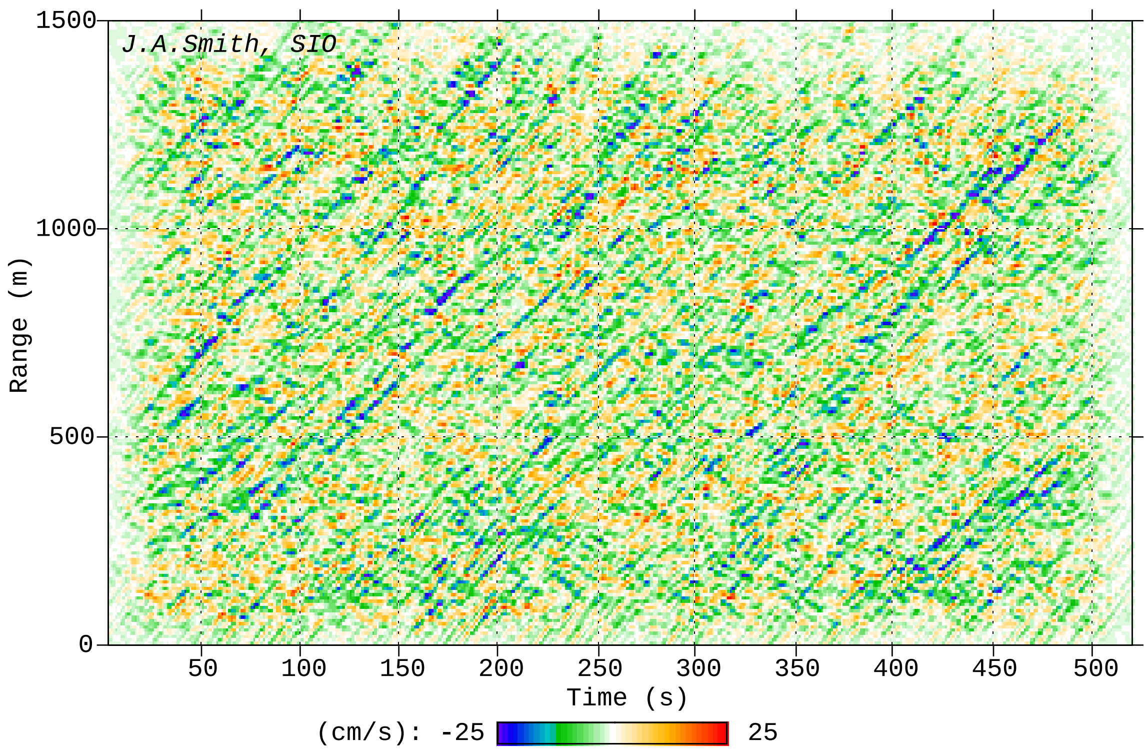

Figure 16. Time-range plot of the wave-filtered radial Eulerian velocity U_0 along one beam. There is a predominance of blue slashes rising to the right, propagating at about 5 m/s. There is some resemblance to the red slashes seen in the plot of Stokes drift (figure 15).

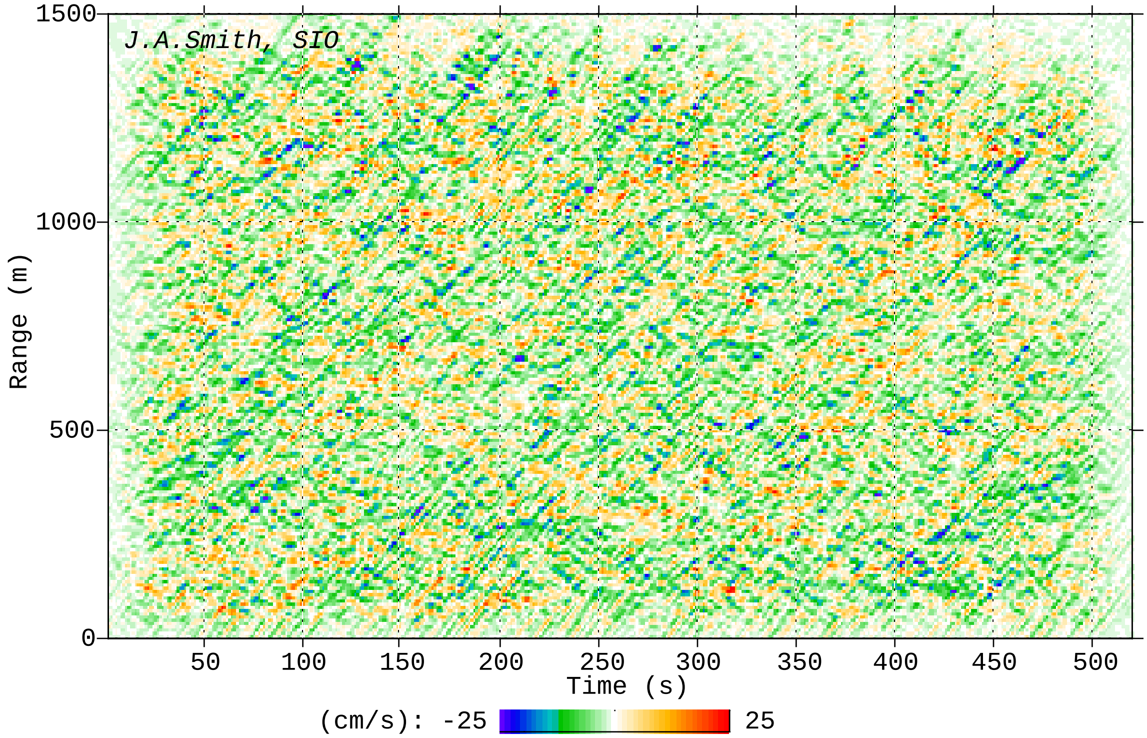

Figure 17. Time-range plot of the wave-filtered radial Lagrangian velocity $U_L = U_0 + U_S$ for the same data as figure 18. The cancellation of variance is quite complete at all resolved scales, leaving essentially an image of the filtered measurement noise.

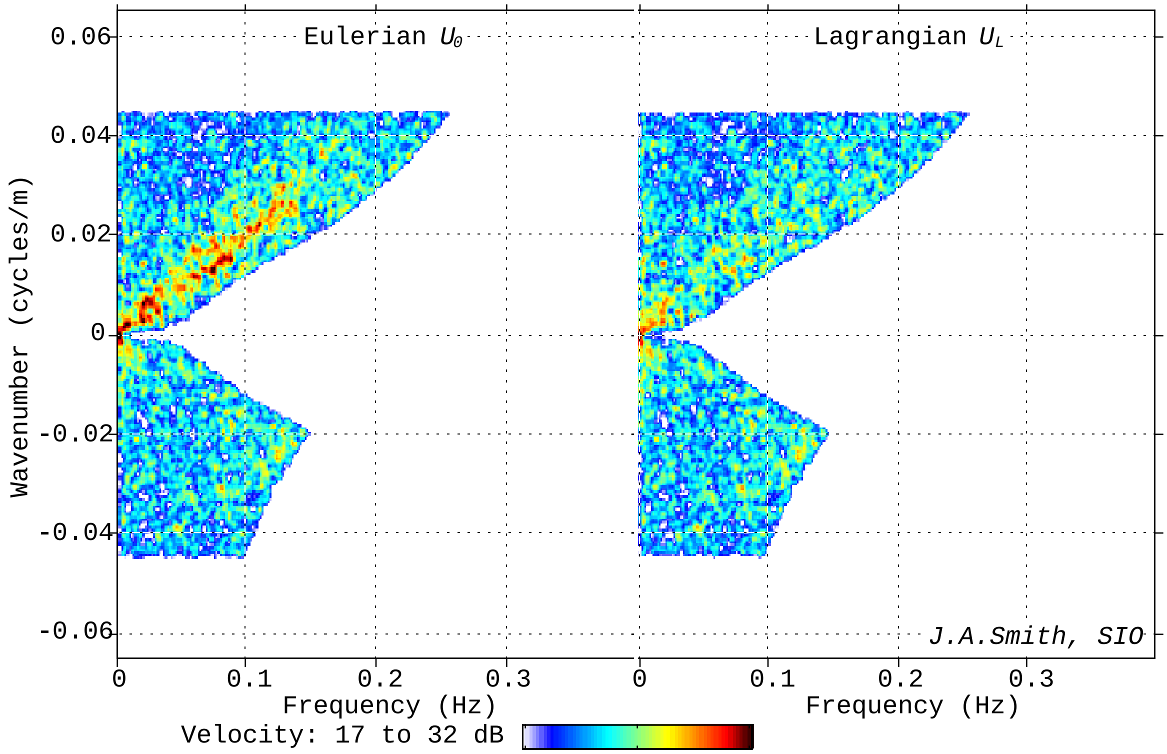

Figure 18. Wavenumber-frequency spectra for (left) the Eulerian velocity field and (right) the Lagrangian velocity field formed by adding the Eulerian and Stokes drift estimates. The reduction in variance along the 5 m/s line in the Lagrangian field is dramatic. Because the means are not well determined, some variance is to be expected near the origin. Comparison of the spectral levels at + and – *k* values for the same frequencies indicates that there is no longer any preferential direction; the remainder probably represents the spectral noise floor. In particular, note that there is no significant signal in the Lagrangian spectral densities for wavenumbers over roughly 0.005 cycles/m.

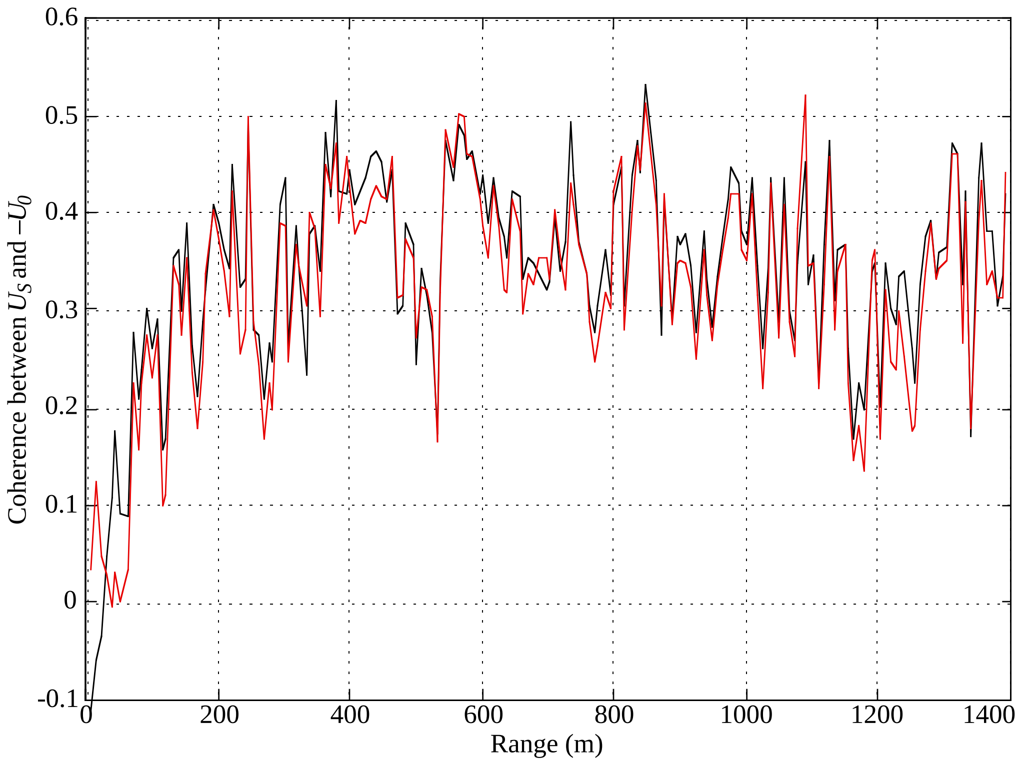

Figure 19. Coherence between U_S and $-U_0$ versus range, as estimated from time averages: $-\langle U_S U_0 \rangle / [\langle U_S^2 \rangle \langle U_0^2 \rangle]^{1/2}$ (both for wave-filtered velocities; note minus sign). As indicated by the level of jitter, the standard deviation of the coherence estimate is less than 0.1. The 95% level is about 0.12, and the coherence levels are several times larger than this.

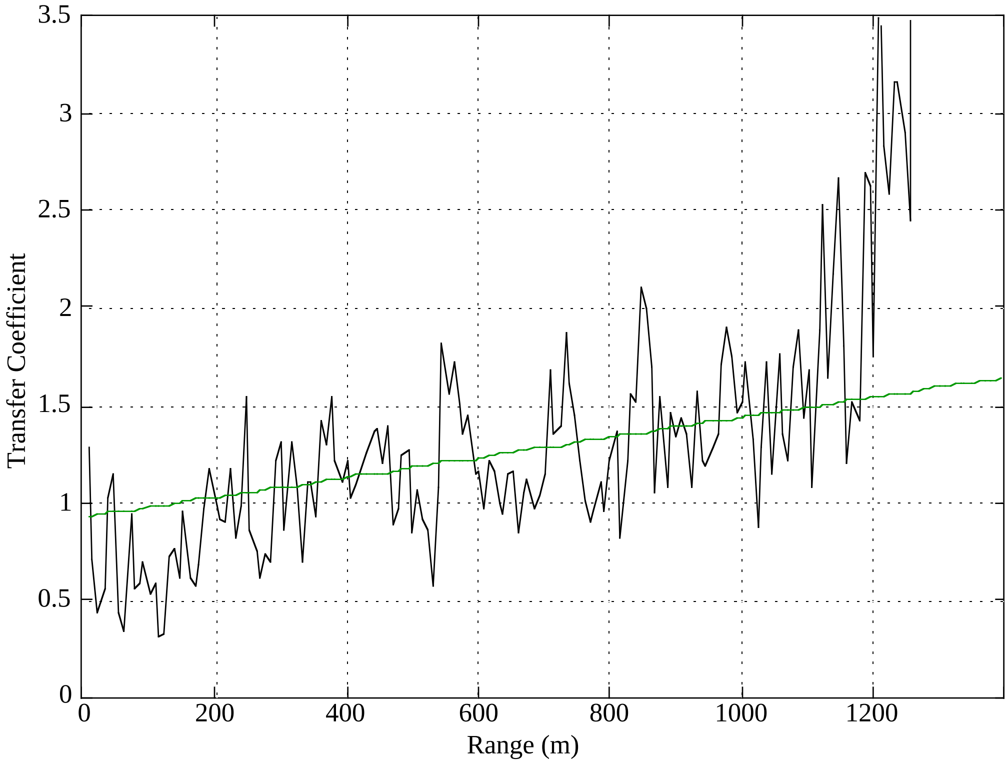

Figure 20. The transfer coefficient from Stokes drift U_S to the negative Eulerian velocity anomaly (wave-filtered) $-U_0$: $T_C = -<U_S U_0>/<U_S^2>$. This starts very near 1.0 at near ranges, indicating that the correlated part of the two fields cancel out. A value over 1 indicates an Eulerian anomaly larger than the Stokes drift, contrary to expectations. As range increases, the Stokes drift is probably underestimated slightly due to finite spatial smoothing. The increase in transfer coefficient with range is likely attributable to this, and might serve as a guide in compensating for this underestimation (see figure 13). There is every indication that the response is no smaller than the Stokes drift, and is most likely a one-to-one match.